Behavioral/Systems/Cognitive

Gateways of Ventral and Dorsal Streams in Mouse Visual Cortex

Quanxin Wang, Enquan Gao, and Andreas Burkhalter
Department of Anatomy and Neurobiology, Washington University School of Medicine, St. Louis, Missouri 63110

It is widely held that the spatial processing functions underlying rodent navigation are similar to those encoding human episodic memory (Doeller et al., 2010). Spatial and nonspatial information are provided by all senses including vision. It has been suggested that visual inputs are fed to the navigational network in cortex and hippocampus through dorsal and ventral intracortical streams (Whitlock et al., 2008), but this has not been shown directly in rodents. We have used cytoarchitectonic and chemoarchitectonic markers, topographic mapping of receptive fields, and pathway tracing to determine in mouse visual cortex whether the lateromedial field (LM) and the anterolateral field (AL), which are the principal targets of primary visual cortex (V1) (Wang and Burkhalter, 2007) specialized for processing nonspatial and spatial visual information (Gao et al., 2006), are distinct areas with diverse connections. We have found that the LM/AL border coincides with a change in type 2 muscarinic acetylcholine receptor expression in layer 4 and with the representation of the lower visual field periphery. Our quantitative analyses also show that LM strongly projects to temporal cortex as well as the lateral entorhinal cortex, which has weak spatial selectivity (Hargreaves et al., 2005). In contrast, AL has stronger connections with posterior parietal cortex, motor cortex, and the spatially selective medial entorhinal cortex (Haftig et al., 2005). These results support the notion that LM and AL are architecturally, topographically, and connectionally distinct areas of extrastriate visual cortex and that they are gateways for ventral and dorsal streams.

Introduction

Visual information is used for object recognition, moving eyes and head, reaching, grasping, and navigation (Whitlock et al., 2008). It is widely held that these functions rely on basic spatial processing mechanisms that are similar to those used for encoding episodic memory (Knierim et al., 2006; Bird and Burgess, 2008; Eichenbaum and Lipton, 2008; Doeller et al., 2010). The neuronal network that underlies these functions is known to interconnect the visual cortex with somatosensory, posterior parietal, motor, temporal, and parahippocampal areas as well as the hippocampus (Bird and Burgess, 2008; Whitlock et al., 2008).

Navigation relies on the perception of landmarks and the processing of path integration information about the speed and the direction of self-motion (Whitlock et al., 2008). The task of the visual system, then, is to deliver nonspatial information about landmarks and spatial information about their topographic relationships including cues about self-location to the network. In the primate visual system, this diverse information is carried by interconnected streams that preferentially link areas in ventral and dorsal cerebral cortex (Ungerleider and Mishkin, 1982; Goodale, 2010). It has been proposed that circuits in the rodent visual system are organized in similar fashion (Kolb, 1990; McDonald and Mascagni, 1996). However, there is little detailed understanding of the network that carries different forms of visual information from V1 to temporal, posterior parietal, and motor cortex.

Classic studies have shown that mouse V1 sends output to two regions in medial and seven regions in lateral extrastriate visual cortex (Olavarria and Montero, 1989). In rats and mice, the strongest inputs terminate on the lateral side of V1 at two sites within an island that receives few callosal inputs (Coogan and Burkhalter, 1993; Wang and Burkhalter, 2007). Topographic mapping studies of connections from V1 and recordings of receptive fields have shown that each of these regions contains complete representations of the contralateral visual field that belong to separate areas, the lateromedial field (LM) and anterolateral field (AL) (Wang and Burkhalter, 2007). Both of these areas have also been identified by mapping of intrinsic optical signals (Schuett et al., 2002; Tohmi et al., 2009). Based on the distinctive connections and the shared vertical meridian representation with V1, it was suggested that LM corresponds to primate V2 (Coogan and Burkhalter, 1993; Wang and Burkhalter, 2007). Although differences in neurofilament, serotonin, and cytochrome oxidase expression were found in lateral extrastriate cortex (Remple et al., 2003; Hamasaki et al., 2004; Van der Gucht et al., 2007), it remains unclear whether LM and AL are chemoarchitectonically distinct. Recordings indicate that LM and AL are functionally diverse (Gao et al., 2006), suggesting that high spatial resolution information flows through LM to temporal cortex, whereas information about fast-moving objects flows through AL into the

Received July 5, 2010; revised Nov. 17, 2010; accepted Dec. 3, 2010.

This work was supported by National Eye Institute Grant R01EY016184, the McDonnell Center for System Neuroscience, and the Human Frontier Science Program 2000B. We thank Justin Horowitz for developing Matlab software and Katia Valkova for excellent technical assistance. The content of this manuscript is solely the responsibility of the authors and does not necessarily represent the official views of the National Eye Institute or the National Institutes of Health.

Correspondence should be addressed to Andreas Burkhalter, Department of Anatomy and Neurobiology, Washington University School of Medicine, 660 South Euclid Avenue, St. Louis, MO 63110-1093. E-mail: burkhala@pcg.wustl.edu.

DOI:10.1523/JNEUROSCI.3488-10.2011

Copyright © 2011 the authors 0270-6474/11/311905-14$15.00/0

posterior parietal cortex. Here, we examined whether LM and AL are chemoarchitectonically and connectionally distinct. The results show an abrupt decrease in type 2 muscarinic acetylcholine receptor (m2AChR) expression at the LM/AL border. In addition, distinctive pathways suggest that LM is a gateway to the ventral stream, whereas AL preferentially provides inputs to the dorsal stream.

Materials and Methods

Experiments were performed in postnatal day 10 (P10) and 6- to 8-week-old C57BL/6J male and female mice. All experimental procedures were approved by the Institutional Animal Care and Use Committee at Washington University and conformed to the National Institutes of Health guidelines.

Mapping chemoarchitecture of cortex

For mapping the chemoarchitecture, we have used immunostaining of different markers together with retrograde labeling of callosal connections in tangential sections of flatmounts of the left cerebral hemisphere. Sectioning the cortex in the tangential plane is critically important in animals with small brains in which the spatial resolution of graphically reconstructed labeling patterns from coronal sections limits the accuracy of making maps of chemoarchitectonic regions (Paxinos and Franklin, 2001; Van der Gucht et al., 2007). In addition, labeling of callosal landmarks in the same sections is invaluable for assigning chemoarchitectonic fields and connections to specific cortical areas and regions (Wang and Burkhalter, 2007).

Newborn P10 mice were anesthetized by inhalation of 2.5% isofluorane (Butler) in oxygen. Adult mice were anesthetized with a mixture of ketamine (86 mg · kg^{-1}) and xylazine (13 mg · kg^{-1}, i.p) Analgesia in newborns and adults was achieved by injections of buprenorphine (0.05 mg · kg^{-1}, s.c.). For tracer injections, mice were put in a headholder (Stoelting) equipped with an adapter for neonatal animals. The body temperature was maintained at 37°C with a feedback-controlled heating pad. Callosal connections were labeled by making a large craniotomy on the right side and distributing multiple pressure injections (>30) of bisbenzimide (5% in H_2O, 20 nl each; Sigma) in a gird-like fashion (spacing, ~0.5 mm) across the posterior third of cortex. After the injections, the bone was replaced, and the skin flaps were either glued together (Vet Close; Butler; newborns) or closed with wound clips (adults). To prevent cannibalization, the skin and nose of newborns including their mothers were covered with phenol-tainted Vaseline before returning to the cage. Adult mice recovered in a heated chamber and were later returned to the home cage. After 1 d (newborns) or 3 d (adults) survival, mice were perfused through the left ventricle with 0.1 M phosphate buffer (PB; pH 7.4) followed by 1% paraformaldehyde in PB (PFA). Immediately after the perfusion, the brain was removed; the cortex was separated from the rest of the brain and flattened. This was achieved by placing the cortex upside down on a glass slide and covering the tissue with a 3-mm-thick sponge topped by a second glass slide. The assembly was then immersed in 4% PFA overnight at 4°C and equilibrated in 30% sucrose. The flattened cortex was placed pial surface down into Peel-A-Way embedding mold (VWR), which was filled with O.C.T. compound (Electron Microscopic Sciences) and frozen in 90% ethanol cooled with dry ice. Tangential sections were cut at 50 μm on a cryostat. The sections were wet mounted onto glass slides and coverslipped. Retrogradely labeled callosal connections were imaged in the sixth section below the pial surface with a 2× objective under a Nikon 80i microscope equipped with UV fluorescence optics and a cooled CCD camera (Optronics Magnafire). Dark-field illumination of the same section was used to reveal the myeloarchitectonic borders of primary visual, auditory, and somatosensory areas. The sections were then removed from the slides, and complete series of sections from adult mice were immunostained with antibodies against the nonphosphorylated neurofilament SMI-32 protein or the m2AChR. Sections from P11 mice were used to study the transiently expressed type 3 retinoic acid dehydrogenase (RALDH3) (Luo et al., 2004), which is mostly undetectable in 60-d-old mice (Wagner et al., 2006). Floating sections were preincubated in PB containing 5% normal goat serum and 0.3% Triton X-100 for 4 h and treated with mouse anti-SMI-32 (1:5000 in PBS, SMI32R; Convance), rat anti-m2AChR (1:500 in PBS, MAB367; Millipore), or rabbit anti-RALDH3 (1:4000 in PBS; gift from U. C. Dräger, Eunice Kennedy Shriver Center for Mental Retardation, Waltham, MA). This step was followed by a 4 h incubation (20°C) in biotinylated goat anti-mouse (1:400; Jackson ImmunoResearch), goat anti-rat (1:400; Jackson ImmunoResearch), or biotinylated goat anti-rabbit (1:400; Jackson ImmunoResearch) secondary antibodies and an ABC reaction with avidin and biotinylated HRP (Vectastain ABC Elite) in the presence of diaminobenzidine (DAB; 0.05%) and H_2O_2 (0.01%). Finally, the DAB reaction product was intensified with $AgNO_3$ and $HAuCl_2$ (Jiang et al., 1993). The expression patterns of SMI-32, m2AChR, and RALDH3 were imaged and digitally

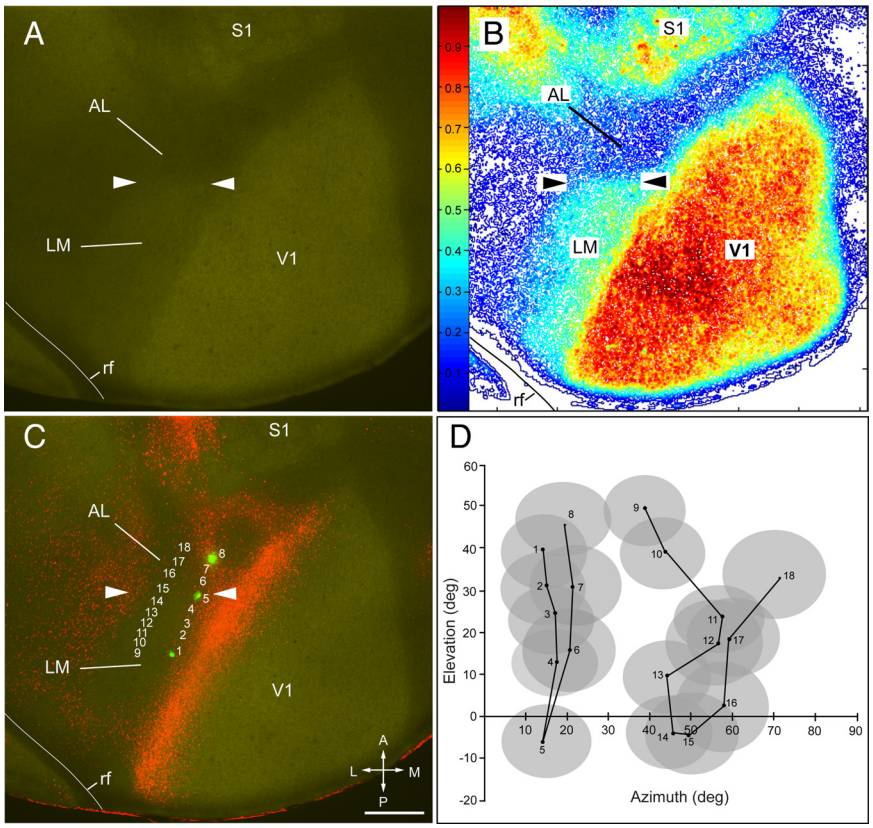

Figure 1. LM/AL border identified by the transition of m2AChR expression coincides with receptive field recordings from lower visual field. ***A***, Expression of m2AChR in a tangential section through layer 4 in left adult visual cortex. The arrowheads mark the LM/AL border between the m2AChR-expressing area LM and the nonexpressing area AL. ***B***, Density contour map of m2AChR expression showing a ≥20% reduction of immunostaining at the LM/AL border (arrowheads). ***C***, ***D***, Overlay of m2AChR with FR-labeled callosal connections. Numbered rows in ***C*** indicate recording sites in areas LM and AL. The receptive fields at site 1 (posterior green mark) are in the upper visual field (***D***), drop to the lower visual field (site 5, middle green mark) at the LM/AL border (***C***, ***D***, arrowheads), and reverse back to upper fields (site 8, anterior green mark) in AL (***C***, ***D***). A second series of recordings (sites 9–18) shows a similar trend with a reversal at site 15. Note that the recordings sites 5 and 15 coincide with the transition in m2AChR expression (arrowheads), showing that the LM/AL border represents the lower visual field periphery, which was previously identified as the boundary between areas LM and AL (Wang and Burkhalter, 2007). rf, Rhinal fissure; A, anterior; M, medial; P, posterior; L, lateral. Scale bar, 0.5 mm.

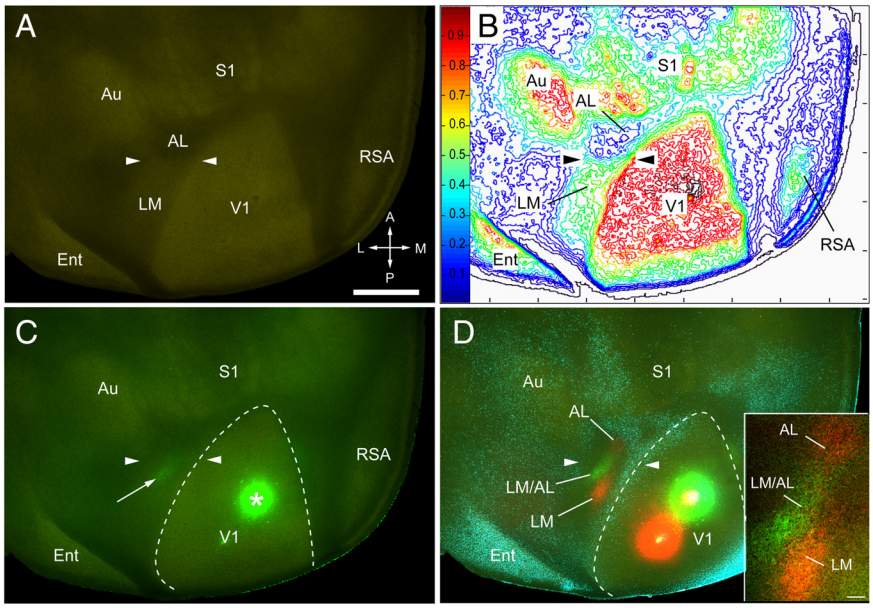

Figure 2. Chemoarchitectonic LM/AL border identified by m2AChR expression and connections from lower visual field of V1. ***A***, m2AChR expression in tangential section through layer 4 of left adult cerebral cortex, showing an abrupt decrease in labeling intensity in the belt on the lateral side of V1 (arrowheads). ***B***, Density contour map of m2AChR expression showing a ≥20% reduction of immunostaining at the LM/AL border (arrowheads). ***C***, Overlay of m2AChR (green-yellow immunolabeling) with lower field input from V1 labeled by anterograde transport after injection of FE into V1 (asterisk). The bright green projection (arrow) coincides with the LM/AL border marked by arrowheads. ***D***, Overlay of m2AChR expression with the projections from the lower quadrant of the visual field of V1 (green FE-labeled axons), the upper quadrant of V1 (red FR-labeled axons), and callosal connections (blue bisbenzimide-labeled cell bodies). The red (FR) and green (FR) spots in V1 mark the injection sites. The yellow centers indicate dye saturation at the center of injection sites. Note that the green projection from the lower field labels a single site that coincides with the LM/AL border (arrowheads) marked by m2AChR expression (***C***). Inset, Lower field projection from V1 (green) to the LM/AL border is flanked by two red clusters from the upper field of V1 terminating in LM and AL. Ent, Entorhinal cortex; A, anterior; M, medial; P, posterior; L, lateral. Scale bars: ***A***, 1 mm; ***D***, inset, 0.1 mm.

aligned (Photoshop CS2; Adobe) with the callosal pattern using blood vessels as reference.

Anatomical mapping of LM/AL border. For localizing the border between areas LM and AL, we used topographic mapping with anterograde and retrograde tracers combined with immunolabeling of m2AChR and Nissl staining. Adult mice were anesthetized and secured in a headholder as described above. Pressure injections of the anterograde tracers Fluororuby (FR; 5% in H_2O, 20 nl; Invitrogen) or Fluoroemerald (FE, 5% in H_2O, 20 nl; Invitrogen) or retrograde tracers (20 nl of rhodamine- or fluorescein-labeled latex microspheres; Lumafluor; Retrobeads) were made 300 μm below the pial surface in the upper and lower visual field representation of V1, using glass pipettes (tip diameter, 15 μm) connected to a Picospritzer (Parker-Hannafin). Upper visual field injections were made 3 mm lateral to the midline and 1.1 mm in front of the anterior margin of the transverse sinus. Lower field injections were 2.6 mm lateral to the midline and 2 mm in front of the anterior margin of the transverse sinus. Callosal connections were labeled with bisbenzimide from the opposite hemisphere, as described above. After 3 d of survival, mice were perfused with 1% PFA, and *in situ* images of the callosal labeling pattern as well as the FR, FE, and microsphere injection sites were taken under a stereomicroscope equipped for UV, fluorescein, and rhodamine fluorescence (Leitz MZ16F) and a CCD camera (CoolSnap EZ) (Wang et al., 2007). The cortex was then flattened, postfixed in 4% PFA, and equilibrated in 30% sucrose. Cryostat sections were cut at 50 μm either in the tangential or quasi parasagittal plane. The sections were wet mounted, and the bisbenzimide-labeled callosal, FR, FE, or microsphere-labeled ipsilateral connections were imaged under a Nikon 80i fluorescence microscope equipped with UV, fluorescein, rhodamine, and infrared (IR) fluorescence optics. The sections were then removed from the slides and immunostained with rat anti-m2AChR (1:500) primary antibody followed by goat anti-rat Alexa 647 (1:400 in PBS, A21247; Invitrogen) secondary antibody. The sections were wet mounted again, and the m2AChR expression was imaged under IR fluorescence illumination and digitally aligned with the callosal, FR, FE, and microsphere labeling patterns. Next, the sections were stained with cresyl violet for Nissl substance. Nissl staining was imaged under bright-field illumination and digitally aligned with the fluorescent callosal and ipsilateral connection patterns.

Electrophysiological mapping of LM/AL border. To link architectural borders with the visuotopic organization of areas LM and AL, we performed receptive field mapping in the large acallosal region on the lateral side of V1. The callosal connections were labeled by multiple pressure injections of FR (20 nl each 5% in H_2O; Invitrogen) into the right occipital cortex. Three days later, mice were anesthetized with urethane (1.2 g/kg in 20% saline solution, i.p.) and secured in a customized headholder. The bone over the left visual cortex was thinned to reveal the FR-labeled callosal connections, using transcranial imaging with a stereomicroscope equipped with rhodamine optics (Wang et al., 2007). The large acallosal zone on the lateral side of V1 was then exposed, and multiunit recordings of receptive fields were made in LM and AL. Recordings were performed with lacquer-coated tungsten microelectrodes (1–1.5 MΩ). Neuronal signals were bandpass filtered from 300 to 5000 Hz, using the Axoprobe-2A amplifier (Molecular Devices). Selected recording sites were marked by painting recording electrodes with FE (5% in H_2O; Invitrogen).

Visual stimulation was performed with a flat screen color monitor, which was mounted on an adjustable stand at 30 cm viewing distance (Gao et al., 2010). The stimuli were viewed with the right eye from a position in which the incisor bar was 2.5 mm below the interaural line and the roof of the mouth was horizontal. The nose was aligned with the vertical meridian, and the horizontal meridian intersected the center of the pupil. The eyes were kept moist with a thin layer of ophthalmic ointment (Paralube). No attempt was made to restrain eye movements, because previous studies in anesthetized mice have shown that eye movements are extremely small and negligible considering the large receptive fields in LM and AL (Dräger, 1975; Wagor et al., 1980; Gordon and Stryker, 1996; Wang and Burkhalter, 2007). To search for visual responses, we moved a slit on the screen with a computer mouse and listened to the responses on an audiomonitor. A mapping program was then used to plot the spike rates and qualitatively outline the receptive field. For quantitative analysis of receptive field size, a circular patch (5° in diameter) of a drifting grating (5°/s, 0.03 cycles/degree) was displayed for 2 s at various locations on the screen. This procedure generated spatial response plots in which points with similar mean response strengths were connected by contour lines (Gao et al., 2010). The contour corresponding to 2 SDs of the fitted Gaussian represented the size of the receptive field. Receptive field location was determined by measuring azimuth and elevation of its center to the eye with a digital protractor.

At the end of the recording session, mice were perfused, and the cortex was flattened and sectioned tangentially as described above. FR-labeled callosal connections and FE-marked recording sites were imaged under a microscope equipped with rhodamine and fluorescein fluorescence optics. Interpolation of marked recording sites was used to plot unlabeled recording sites onto the cortex.

Mapping intracortical connections. For mapping intracortical connections of LM and AL, we combined anterograde tracing of axons with biotinylated dextran amine (BDA) in the left cerebral cortex with retrograde bisbenzimide tracing of callosal connections from the right hemisphere. Labeling of callosal connections provided landmarks that were

critically important for the identification of extrastriate visual areas (Wang and Burkhalter, 2007). Adult mice were anesthetized and secured in a headholder (see above). Ipsilateral cortical connections were labeled by injecting BDA (10,000 molecular weight, 5% in H_2O, 20 nl; Invitrogen) 300 and 500 μm below the pial surface, using glass pipettes (tip diameter, 15 μm) connected to a Midgard iontophoresis current source (Stoelting). Injections were made by applying 3 μA at a 7 s on/off duty cycle for 10 min. The stereotaxic coordinates for LM injections were 4.1 mm lateral of midline and 1.4 mm in front of the anterior margin of the transverse sinus. AL injections were made 3.7 mm lateral and 2.4 mm in front of the transverse sinus. Callosal connections were labeled by making a large craniotomy on the right side and distributing multiple pressure injections of bisbenzimide across the occipital cortex (see above). At the end of the injections, the wound was closed with clips. Mice recovered in a heated chamber and were later returned to the home cage. After 3 d of survival, mice were perfused with 1% PFA, the cortex was flattened and postfixed in 4% PFA and equilibrated in 30% sucrose. Tangential sections were cut on a cryostat at 50 μm. The sections were wet mounted and coverslipped, and bisbenzimide-labeled callosal connections were imaged (see above). The sections were then removed from the slides, treated with 0.3% Triton X-100 in PB, and stained with avidin and biotinylated HRP (Vectastain ABC Elite) in the presence of DAB (0.05%) and H_2O_2 (0.01%). The DAB reaction product was intensified with $AgNO_3$ and $HAuCl_2$ (Jiang et al., 1993). BDA-labeled connections were imaged under dark-field illumination and digitally superimposed with the callosal landmarks.

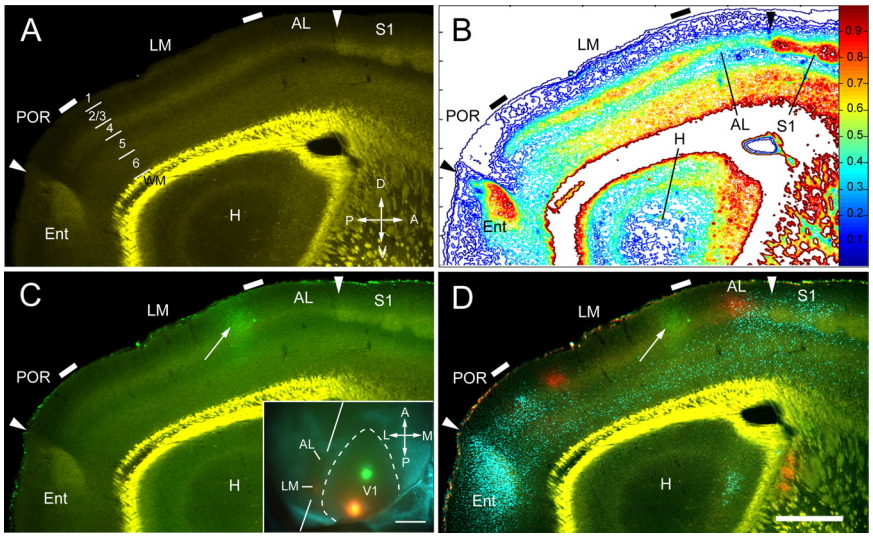

Figure 3. Chemoarchitectonic LM/AL border shown by m2AChR expression in parasagittal section coincides with V1 inputs from lower visual field. ***A***, m2AChR expression in parasagittal section showing moderate to strong immunofluorescence in layers 1, 2, 4, deep 5, and 6 of areas LM and AL. Note the transition in the thickness of layer 4 at the LM/AL and LM/POR borders (tick marks). The posterior arrowhead indicates the border between POR and entorhinal cortex (Ent). The anterior arrowhead marks the AL/S1 border. Bright yellow represents nonspecific labeling of myelinated fibers in white matter. A, anterior; V, ventral; P, posterior; D, dorsal. ***B***, Density contour map of m2AChR expression showing a ≥20% reduction of immunostaining and a decrease in the width of staining in layer 4 that coincides with the LM/AL border (tick mark). ***C***, Overlay of anterogradely FE-labeled connections from the lower field of V1 shows that the green projection site (arrow) is aligned with a transition in the width of m2AChR staining in layer 4 that coincides with the LM/AL border. Inset, *In situ* image of green and red injection sites into V1. The blue pattern represents callosal projections. The oblique lines indicate the plane of quasi parasagittal sectioning. A, anterior; M, medial; P, posterior; L, lateral. Scale bar, 1 mm. ***D***, Overlay of m2AChR expression (faint green/yellow staining) with V1 projections from lower (green, FE) and upper (red, FR) fields and callosal connections (blue, bisbenzimide). Note that the green projection (arrow) coincides with the LM/AL border (tick mark). The posterior red projection is near the posterior border of the acallosal region (i.e., border with POR), whereas the anterior red projection falls into AL. The bright yellow color represents nonspecific staining of white matter. H, Hippocampus; Ent, entorhinal cortex. Scale bar, 0.5 mm.

Data analysis

To quantitatively assess the chemoarchitecture of m2AChR, SMI-32, and RALDH3 expression and the cytoarchitecture of Nissl-stained tissue, we have analyzed staining density in sections with customized Matlab (MathWorks) software. For this purpose, digital gray-tone images were used to determine maximum and minimum staining densities in regions of interest. The images were then filtered with a Gaussian at 5 μm, blood vessels were subtracted from the images, and density contours were plotted by thresholding at 20% intervals. The contours were displayed as heat maps that showed the distribution of staining densities in horizontal and parasagittal sections through the cortex.

The density of Nissl staining across cortical layers was determined by line scans of optical density (MetaMorph; Molecular Devices) and averaging across three different sections from five different mice.

The strength of BDA-labeled projections was assessed by counting boutons and optical densitometry. Because the projection strength (i.e., weight) depends on the size and location of the injection site, both bouton and projection densities were expressed as functions of the total BDA-labeled output of V1. Both measurements were made in tangential sections.

Bouton counts were performed with a 100× oil-immersion lens, using the optical dissector as a stereological probe for systematic random sampling of objects provided by Stereo Investigator software (MicroBrightfield). For each connection, we used custom-made Matlab software to generate a contour map that revealed 80% of the BDA-labeled projection field. Within this region, we then randomly selected four sections at different levels across the superficial 350 μm of cortex and counted boutons in 15 × 15 μm frames at 60–160 sampling sites, distributed with an average spacing of 46 μm, in a volume of 4000–6000 μm^3. The Scheaffer correlation coefficient was used to assess whether the number of boutons counted per frame was a significant ($p < 0.05$) representation of the strength of whole projection. The sum of boutons across all projections was then taken as 100% and used for expressing the strength of individual connections in percentage of the total BDA-labeled V1 output. Measurements from three mice were averaged (±SEM) and plotted against relative projection densities.

For densitometric measurements of the projection strength, we used bright-field images taken with a 4× objective and analyzed the images with custom-made Matlab software. The density of each projection was determined relative to the center of the injection site (i.e., darkest region of the specimen) and was scaled to the unstained background at the projection site. Blood vessels were subtracted from the image, and a 5 μm Gaussian blur was applied. To calculate a weight index, the density measurements of all projections labeled by a given injection were summed, and the strength of each projection was expressed as the percentage of the total BDA-labeled output of V1. Mean relative density measurements (±SEM) from three mice were averaged and plotted against mean relative bouton counts. The plot was fitted by linear correlation analyses. The statistical significance of R^2 was $p < 0.05$. Identical density measurements were made to compare the projections strengths of extrastriate visual areas. The *t* test was used for statistical comparisons. Significance was set at $p \leq 0.05$.

Results

Chemoarchitectonic and cytoarchitectonic borders coincide with topographic LM/AL border

In immunostained horizontal sections through layer 4, we found dense m2AChR expression in V1 and weaker staining in surrounding extrastriate cortex (Fig. 1*A*). The weakly stained extrastriate region was most obvious on the lateral side of V1, where it

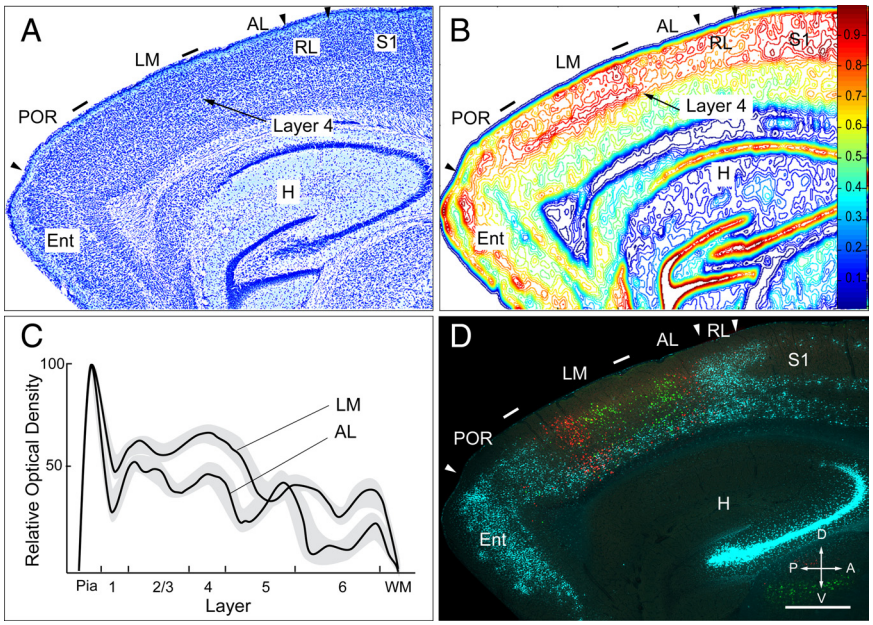

Figure 4. Cytoarchitectonic LM/AL border coincides with lower visual field input from V1. ***A***, Nissl-stained parasagittal section. Tick marks indicate LM/AL and LM/POR borders. Within LM, there are no clear cytoarchitectonic differences between layers 2/3 and 4. In deep layers of LM, cells are less densely packed. In AL, layer 4 appears more distinct from layers 2/3 and 5. These differences are more readily apparent by marking the LM/AL border through tracing of lower field inputs to V1 (***D***). The arrowheads indicate the POR/Ent, AL/RL, and RL/S1 borders. ***B***, Density contour map of Nissl-stained cell bodies shown in ***A***. The optical density of layers 2–4 of LM is 10–20% higher than in AL. The difference is most prominent in layer 4. The map also indicates that layer 4 in AL is thinner than in LM. ***C***, Line scan of optical density across layers in LM and AL. The average ± SEM (gray regions) density in layers 2–4 of LM is higher and layer 4 is wider than in AL. WM, White matter. ***D***, Fluorescence image of section adjacent to the Nissl-stained section depicted in ***A***, showing retrogradely labeled callosal connections (blue) and microsphere-labeled neurons that project to the upper (red) and lower (green) visual field representation of V1. Both green patches are flanked by two red clusters of neurons at posterior and anterior edge of the acallosal region. Notice that the green patches are closer together on the posterior and anterior sides of the LM/AL border (tick mark) shown in ***A*** and ***B***. H, Hippocampus; Ent, entorhinal cortex; A, anterior; V, ventral; P, posterior; D, dorsal. Scale bar, 0.5 mm.

extended about half the distance from the rhinal fissure to the tip of V1. At this point, the staining density decreased suddenly by ≥20% and marked a border that ran mediolaterally across the acallosal island encircled by FR-labeled callosal connections (Fig. 1*B*,*C*). The bisection of the acallosal island into a posterior and anterior field was reminiscent of areas LM and AL (Wang and Burkhalter, 2007) and suggested that m2AChR expression marked the LM/AL border. To test this possibility, we recorded receptive fields, labeled selected positions by small deposits of FE, and correlated their location with immunostaining for m2AChR. The results in Figure 1*C* show that in the medial recording sequence (sites 1–8), receptive field positions dropped from the upper to the lower nasal visual field and at site 5 reversed to the upper nasal field (Fig. 1*D*). In the lateral sequence (sites 9–18), we found a similar map inversion at recording site 15 in the temporal visual field (Fig. 1*D*). The map inversion coincided with a slight increase in receptive field size. Moreover, the map inversion at the lower visual field periphery was precisely aligned with a transition in m2AChR expression (Fig. 1*A*–*C*), which strongly indicated that it represented the LM/AL border.

Because it is not always practical to identify the LM/AL border by mapping receptive fields, we studied the relationship of m2AChR expression by mapping axonal input from V1 with anterogradely transported FR and FE. We found that FE injections into the lower visual field always labeled a single green cluster of axon terminals in the center of the large acallosal region on the lateral side of V1 (Fig. 2*C*). This patch was flanked on the anterior and posterior sides by two red projections from the upper visual field (Fig. 2*D*). Importantly, immunostaining of the same section showed that the green patch coincided with the m2AChR border, whereas the red patches fell into either the heavily or weakly m2AChR-expressing regions on either side of the border (Fig. 2*A*–*C*).

To obtain a better view of m2AChR expression in different cortical layers, we performed a similar tracing experiment in brains that were sectioned in the parasagittal plane. As expected, the green projection from the lower quadrant of V1 (Fig. 3*C*, inset) consisted of a single patch that coincided with the transition between LM and AL from a thick to a thin m2AChR-expressing layer 4 (Fig. 3). The red V1 projections from the upper visual field (Fig. 3*C*, inset) labeled a posterior patch in LM and an anterior patch in AL (Fig. 3*D*).

The discovery of an area-specific chemoarchitecture raised the question whether LM and AL are also cytoarchitectonically distinct. At first glance, Nissl-stained sections revealed no obvious differences. However, when we labeled the LM/AL border by retrograde tracing of lower field projections to V1 with green microspheres (Fig. 4*D*), we were able discern a subtle change of cytoarchitecture. For example, in the case shown in Figure 4, we noticed a change in the crispness of the layer 4/5 border between the green-labeled patches representing the lower visual field periphery in LM and AL (Fig. 4*A*,*D*). The transition was quite sudden, changing from a uniform cytoarchitecture in LM to a more laminated pattern in AL (Fig. 4*A*). Similar cytoarchitectonic differences were observed in published atlases (Franklin et al., 2007; Dong, 2008). The change was more readily apparent in line scans where the optical density of layer 4 in LM was ≥20% greater than in AL (Fig. 4*B*,*C*). In addition, density contour maps gave the distinct impression that layer 4 in LM was more densely packed and wider than in AL (Fig. 4*B*). These differences strongly suggest that LM and AL are cytoarchitectonically and chemoarchitectonically distinct areas.

Identification of cortical areas and regions

Cortical areas are constructs that have unique functional properties, architectural features, topographies, and connections (Felleman and Van Essen, 1991). To understand the network of connections between areas, we need unambiguous markers of their borders and identity (Rubinov and Sporns, 2010). This is particularly important in small animals in which cortical cytoarchitecture is relatively uniform and reconstructing two-dimensional maps of small areas (Wang and Burkhalter, 2007) from transverse sections is extremely challenging (Paxinos and Franklin, 2001). Previously, we have used topographic mapping of V1 connections and the relationships of these iputs to fixed callosal connections for delineating at least 10 areas in mouse visual cortex (Wang and Burkhalter, 2007). Topographic mapping of connections and receptive fields, however, is not always practical, and callosal connections by themselves are insufficient for determining areal borders. A more effective approach is using chemoarchitec-

tonic borders. Such borders were found in mice, monkey, and human by the expression of SMI-32, m2AChR, and RALDH3 (Wagner et al., 2006; Saleem et al., 2007; Van der Gucht et al., 2007; Eickhoff et al., 2008). However, whether these chemoarchitectonic borders are correlated with borders of topographic maps that correspond to cortical areas remains unknown.

SMI-32 expression

V1 was identified by strong SMI-32 expression in layer 4 and very weak labeling in the transversely cut upper layers at the posterior border (Fig. 5*A*,*B*). Even stronger SMI-32 expression was found in the primary somatosensory cortex (S1), in auditory cortex (Au), agranular retrosplenial cortex (RSA), and medial entorhinal cortex (MEC) (Fig. 5*A*,*B*). Less dense labeling was observed in the belt surrounding V1. Superimposition of SMI-32 labeling and callosal connections suggested that this belt contained areas P (posterior), POR (postrhinal), LM, LI (laterointermediate), AL, RL (rostrolateral), A (anterior), AM (anteromedial), and PM (posteromedial), in each of which we have previously found a complete topographic map of the visual field (Wang and Burkhalter, 2007) (Fig. 5). Labeling throughout the belt was not uniform. Some of this heterogeneity was caused by sectioning the posterior pole in the transverse plain. This affected mainly the posterior area P, which showed weak labeling in upper layers next to strong labeling in layer 4. In AL, RL, and A, which were cut perfectly tangentially, however, SMI-32 expression in layer 4 was slightly weaker than in LM, suggesting a tentative border between posterior (V2LP) and anterior (V2LA) lateral V2 (Van der Gucht et al., 2007). Still weaker SMI-32 expression was found in AM and PM of the medial acallosal cortex (Wang and Burkhalter, 2007) (Fig. 5). This region was flanked by the unlabeled strip of the mediomedial region (MM), which filled the gap to RSA (Fig. 5). Finally, weak labeling was found at the ventral tip of the SMI-32-expressing band on the lateral side of V1. By location and shape, this sparsely labeled region resembled area 36p, whose inputs from V1 seems to lack topographic organization (Wang and Burkhalter, 2007). Thus, although the SMI-32-expressing belt around V1 included at least nine previously identified areas (Wang and Burkhalter, 2007), the tangential pattern in layer 4 showed no sharp transitions indicative of unambiguous areal borders. However, it is important to note that SMI-32 expression showed conspicuous transitions that may be associated with the A/AM and POR/36p borders.

Moderate SMI-32 expression was found in the cortex that flanked the dorsal side of auditory cortex, which was only partially connected with the opposite hemisphere and filled the gap between Au and S1 (Fig. 5). This region may correspond to the cytoarchitectonically identified third rostral temporal cortex (Te3R) in rat (Palomero-Gallagher and Zilles, 2004). Although SMI-32 expression throughout the region was relatively uniform, clear chemoarchitectonic differences were only apparent in m2AChR-stained sections (Fig. 6*A*,*B*,*D*). This material clearly showed that the region was heterogeneous, composed of the heavily stained dorsal posterior auditory area (DP) (Stiebler et al., 1997; Budinger and Scheich, 2009), the unstained multisensory dorsal anterior area (DA) (Brett-Green et al., 2003), and the secondary somatosensory cortex (S2) (Benison et al., 2007) (Fig. 6).

Very sparse SMI-32 expression was found in the belt that surrounded Au posteriorly and laterally (ventrally) and extended forward along the upper bank of the rhinal fissure (Fig. 5). The SMI-32-negative field included the cytoarchitectonically identified temporal association cortex (TE) and the perirhinal region 36 (Paxinos and Franklin, 2001; Dong, 2008). In rat, TE may correspond to Te2d, in which neurofilament expression is confined mainly to deep layers (Sia and Bourne, 2008), and to Te2C and Te3V (Palomero-Gallagher and Zilles, 2004), which may include the ventral and suprarhinal auditory fields (Higgins et al., 2010). Region 36 may include the cytoarchitectonic fields TeV, Te2v (Palomero-Gallagher and Zilles, 2004; Sia and Bourne, 2008), and Burwell's area 36 (Burwell, 2000). The strongly SMI-32-expressing region in the fundus of the rhinal sulcus, which was cytoarchitectonically distinct from entorhinal cortex (van Groen, 2001), was identified as region 35.

In entorhinal cortex, SMI-32 expression was much denser in the medial (MEC) than the lateral [lateral entorhinal cortex

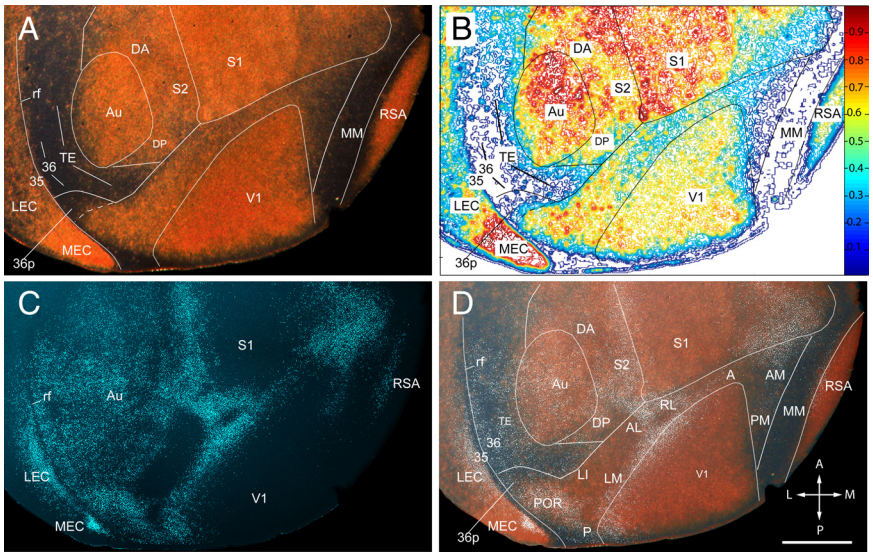

Figure 5. Regional pattern of neurofilament protein (SMI-32) expression in layer 4 of adult mouse cerebral cortex. ***A***, Dark-field image of SMI-32-immunolabeled tangential section showing the posterior half of the left cerebral cortex. The gold-colored labeling shows strong SMI-32 expression in V1 (note that the sections are cut transversely at the posterior pole, which exposes the weakly labeled upper layers), Au, and S1, as well as in RSA and MEC. Moderate SMI-32 expression is found in the cortex between S1 and Au, which contains S2, DP, and DA. Moderate labeling is also observed in LEC and throughout the belt on the lateral side of V1. Much weaker expression is seen in the acallosal region on the medial side of V1. Weak labeling is also found at the lateral (ventral) tip of the belt in a region that corresponds to area 36p. Extremely sparse SMI-32 expression is present in an L-shaped region in TE and the perirhinal areas 36 and 35 on the lateral side of Au. Little detectable SMI-32 expression is seen in a longitudinal MM strip adjacent to RSA. ***B***, Density contour map of SMI-32 expression providing a quantitative image of the staining shown in ***A***. ***C***, Fluorescence image of retrogradely bisbenzimide-labeled callosal connections in the same section shown in ***A***. ***D***, Overlay of SMI-32 labeling shown in ***A*** with white, false-colored callosal connections shown in ***C***. The SMI-32-expressing belt around V1 is shown in an overlay of the fixed pattern of callosal connections. Callosal landmarks were used as reference for identification of areas V1, P, POR, LM, LI, AL, RL, A, AM, and PM, which were previously described by topographic mapping (Wang and Burkhalter, 2007). Labeling in P is nonuniform because of transverse sectioning of weakly labeled upper layers. Labeling of the belt's most lateral tip is weaker and outlines the weakly topographic area 36p (Wang and Burkhalter, 2007). In the rest of the uniformly callosally connected cortex, SMI-32 expression is found in a region that extends from the posterior/dorsal corner of Au into the gap between S1 and Au. This region includes DP, DA, and S2. Very sparse SMI-32 staining is shown in the L-shaped belt on the posterior and lateral side of Au, which includes TE, field 36, and field 35. Extremely sparse staining is present in MM. rf, Rhinal fissure; A, anterior; M, medial; P, posterior; L, lateral. Scale bar, 1 mm.

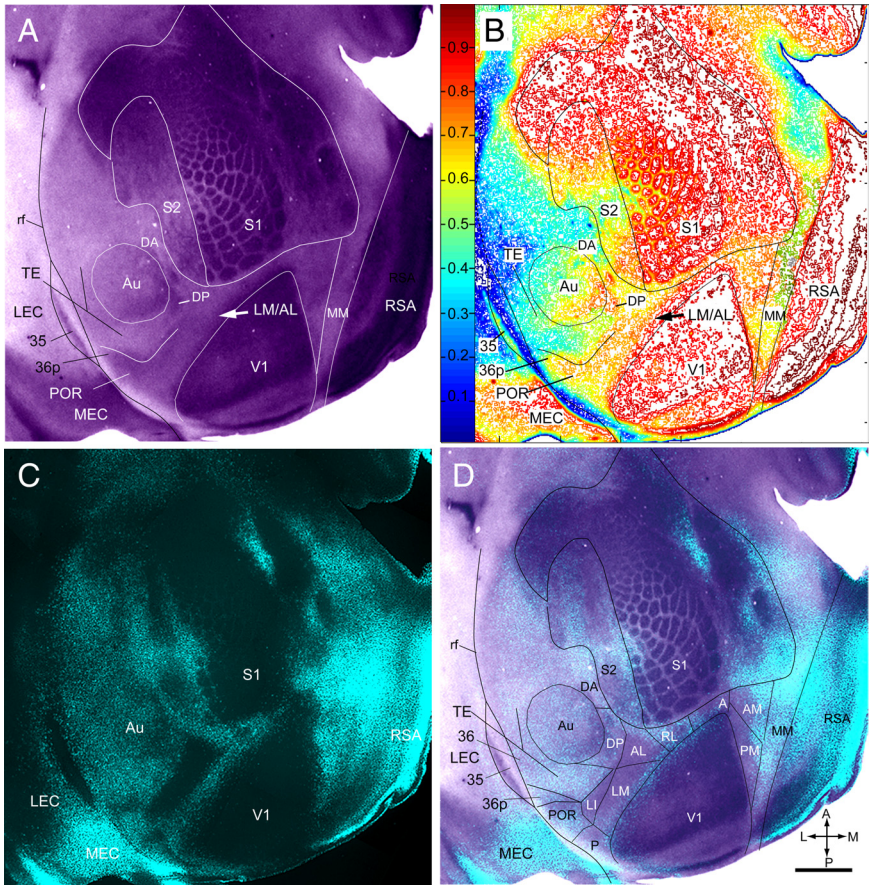

Figure 6. Regional pattern of m2AChR expression in layer 4 of adult mouse cerebral cortex. ***A***, m2AChR-immunolabeled tangential section showing most of the left cerebral cortex. Expression of m2AChR is strong in V1, S1, RSA, and MEC. S2 shows three to five rows of m2AChR-expressing ring-like structures. Moderate staining is found in a belt on the lateral side of V1, extending from 36p to the LM/AL border (arrow) at which the labeling density abruptly decreased and continued around the tip to the medial side of V1. Adjacent to the triangular field on the medial side of V1, we found an unlabeled longitudinal strip, which was previously identified as MM (Wang and Burkhalter, 2007). Moderate nonuniform m2AChR expression is found in Au (identified by myeloarchitectonic borders) and in a region designated DP, adjacent to the posterior/dorsal corner of Au. Weak staining is found on the lateral (ventral) side of Au in intermediate parts of TE and field 36. ***B***, Density contour map of m2AChR expression providing a quantitative image of the staining shown in ***A***). The arrow marks a ≥20% difference in m2AChR expression at the LM/AL border (arrow). ***C***, Fluorescence image of retrogradely bisbenzimide-labeled callosal connections in the same section shown in ***A***. ***D***, Overlay of m2AChR expression shown in ***A*** with callosal connections shown in ***C***. The m2AChR-expressing belt around V1 is shown to overlay the fixed pattern of callosal connections. These landmarks were used as references for identifying areas V1, P, POR, 36p, LM, LI, AL, RL, A, AM, and PM, which were previously described by topographic mapping (Wang and Burkhalter, 2007). Note that m2AChR expression is weaker in AL (better seen in ***A*** and ***B***), which lies in the anterior part of the large acallosal region on the lateral side of V1. Slightly stronger m2AChR expression is observed in acallosal cortex that contains AM and PM on the medial side of V1. In the more uniformly callosally connected cortex, m2AChR expression is present in DP but is absent in DA in the anterior part of the dorsal auditory belt. Very sparse m2AChR staining is present in the L-shaped belt on the posterior and lateral (ventral) side of Au, which includes TE and area 36. Considerable m2AChR expression is found in the acallosal area 35. rf, Rhinal fissure; A, anterior; M, medial; P, posterior; L, lateral. Scale bar, 1 mm.

(LEC)] part (Fig. 5). MEC was distinguished from LEC as the region that, in coronal sections, showed no gap between layers 2 and 3 (van Groen, 2001).

m2AChR expression

The m2AChR expression pattern in layer 4 showed striking similarities with the distribution of SMI-32 labeling. Similar to SMI-32, the most intense m2AChR expression was observed in V1, S1, Au, and RSA (Fig. 6). More moderate m2AChR expression was found in the SMI-32-positive belt around V1 that included areas 36p, POR, P, LI, LM, AL, RL, A, AM, and PM. In the acallosal cortex, which contained AM and PM (Wang and Burkhalter, 2007), m2AChR expression was weak but distinct from the more weakly stained strip of MM that adjoined the lateral side of the heavily labeled retrosplenial cortex (Fig. 6). However, the m2AChR and SMI-32 labeling patterns also showed important differences. For example, in the belt around V1, m2AChR expression continued to the most lateral (ventral) tip where it labeled the triangular area 36p (Fig. 6), in which SMI-32 expression was very weak (Fig. 5). More importantly, m2AChR expression was sharply decreased in the anterior part of the large acallosal region on the lateral side of V1 (Fig. 6), which is consistent with the notion that this chemoarchitectonic transition marks the LM/AL border (Figs. 1*A*–*C*, 2).

Unlike the uniform SMI-32 labeling (Fig. 5) in the gap between S1 and Au, m2AChR expression consisted of several rows of stained ring-like structures (Fig. 6*A*, *B*) reminiscent of an upright vibrissal map, which in rat represents the secondary somatosensory area S2 (Benison et al., 2007). This putative area, S2, extended forward from the posterior margin of S1 to the anterior tip of the barrel field. It received strong callosal connections on the lateral side, which may account for the bilateral forepaw input (Carvell and Simons, 1986). This novel delineation of the secondary somatosensory cortex differs from previous maps of mouse and rat cortex (Wallace, 1987; Remple et al., 2003) in which anterior parts of the lateral parietal region (Fabri and Burton, 1991) overlap with S2. On the lateral side of S2, in the posterior part of the dorsal multimodal sensory zone (Storace et al., 2010), we found a strongly m2AChR-expressing region (Fig. 6) that presumably corresponds to dorsal posterior auditory area DP (Stiebler et al., 1997; Budinger and Scheich, 2009). The same region was also labeled with SMI-32 (Fig. 5). Whereas the anterior DP/DA border was only visible with m2AChR (Figs. 5, 6), both markers unambiguously delineated the posterior DP/TE border (Figs. 5, 6).

In the belt that wrapped around the posterior and lateral (ventral) side of Au, m2AChR expression was generally sparse and resembled the SMI-32-negative belt with a similar shape and location (Fig. 5, 6). The only difference was that in deeper layers, m2AChR expression was increased lateral (ventral) to Au and delineated intermediate regions of temporal and perirhinal cortex, TE and 36 (Fig. 6). Area 35 was identified as an m2AChR-expressing region in the fundus of the rhinal sulcus (Fig. 6).

In entorhinal cortex, m2AChR expression was much denser in the callosally connected than the acallosal part (Fig. 6). The topology of the heavily m2AChR-expressing region resembled the flat map of MEC reconstructed from Nissl-stained coronal sections (Burwell and Amaral, 1998; Hargreaves et al., 2005), suggesting that the more weakly stained subdivision of entorhinal cortex corresponds to LEC.

RALDH3 expression

The expression of RALDH3 showed a regional pattern that was mainly complementary to SMI-32 and m2AChR labeling (Fig. 7). In medial occipital cortex, RALDH3 expression was particularly strong in the callosally connected MM region. Expression in MM was continuous with more anterior regions in cingulate, motor, and prefrontal cortex and resembled the published pattern (Wagner et al., 2006). RALDH3 expression in AM and PM was slightly weaker and gradually decreased toward the medial border of V1. A similar gradual decline in RALDH3 expression was observed across the border with RSA.

A mainly complementary pattern was also found in temporal cortex where RALDH3 strongly labeled the SMI-32- and m2AChR-negative regions of TE and 36 but spared area 35 (Fig. 7). Weaker RALDH3 expression (except in the fundus of the rhinal sulcus) was found in areas 36p, POR, and P, where it partially overlapped with SMI-32 and m2AChR labeling (Fig. 7).

Thus, RALDH3, SMI-32, and m2AChR expression revealed distinct cortical subdivisions at fixed locations, with unambiguous shapes and borders that provided landmarks (similar to callosal connections) that can be used as references for assigning borders of areas and projection targets.

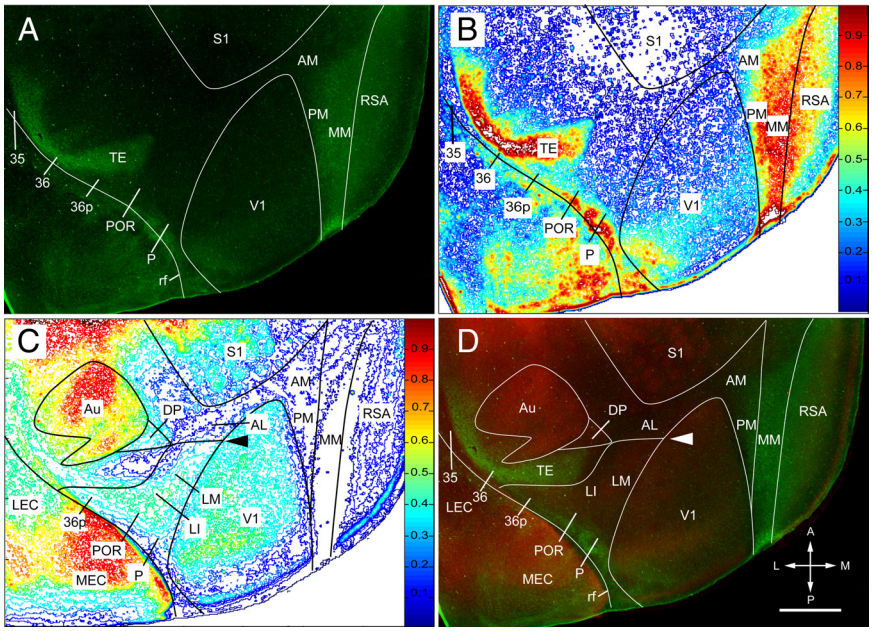

Figure 7. Complementary patterns of RALDH3 and m2AChR expression. ***A***, RALDH3 expression in layer 4 of cerebral cortex in an 11-d-old mouse. Intense staining is found in the center of MM. RALDH3 expression weakens in lateral parts of PM and AM as well as in medial parts of RSA. Strong expression is present in a temporal association (TE) and perirhinal cortex (area 36). Expression of RALDH3 is slightly weaker in posterior parts of P, POR, and 36p close to the rhinal sulcus. No detectable expression of RALDH3 is observed in area 35. ***B***, Density contour map of RALDH3 expression, providing a quantitative image of the staining shown in ***A***. ***C***, Density contour map of m2AChR immunofluorescence of double-immunostained section shown in ***A***. A ≥20% difference in staining intensity is shown at the LM/AL border (arrowhead). ***D***, Overlay of m2AChR (red) and RALDH3 (green) expression in the same section immunolabeled with two different antibodies, showing mainly complementary staining patterns. The LM/AL border is indicated with an arrowhead. rf, Rhinal fissure; A, anterior; M, medial; P, posterior; L, lateral. Scale: 1 mm.

Connections of area LM

In our pathway-tracing experiments, we mostly observed anterogradely labeled axons and only rarely encountered retrogradely BDA-labeled cell bodies. When present, BDA-labeled neurons accounted for less than a single cell per projection site contained in a 50 μm section. We attribute the negligible amount of retrograde transport to the lack of brain injury at the BDA injection site.

We traced the connections of LM in 11 mice. In eight of these, the injection sites were unambiguously located in the posterior/medial part of the large acallosal region on the lateral side of V1 (Fig. 8*A*,*C*,*D*). All of these injections labeled V1 projections that were confined to the upper visual field in the posterior part of primary visual cortex, indicating that the injections were in LM and not in AL (Fig. 8*B*). It is important to note that although the injection sites and sizes (200–500 μm in diameter) appeared variable, V1 projections were always confined to parts of V1, whose locations varied according to the known topographic maps of LM and V1 (Wang and Burkhalter, 2007). For example, injections into posterior LM labeled upper field projections at the posterior edge of V1, in anterior AL, lateral LI, posterior/medial PM, anterior/medial AM, anterior RL, anterior A, and anterior to the rhinal fissure in P and POR (Fig. 8*B*,*D*). In contrast, LM injections of more anterior/lateral sites of the acallosal region labeled lower fields in anterior/medial V1, posterior AL, medial LI, a single large patch at the V1/PM/AM border, RL and A projections at the tip of V1, and P and POR projections at the edge of the rhinal fissure (supplemental Fig. 1, available at www.jneurosci.org as supplemental material).

LM injections labeled 22 distinct cortical targets that differed in projection strength. The main targets in visual cortex were previously identified by topographic mapping of V1 inputs and determining their spatial relationships to callosal connections (Wang and Burkhalter, 2007). These landmarks were traced in the present study and used in each case as fixed references for identifying the projections to V1, P, POR, LI, AL, RL, A, AM, and PM. In the example shown in Figure 8, the connections to V1 terminated in the posterior part of the area, indicating that the injection was located 30–50° in the upper peripheral visual field (Wang and Burkhalter, 2007). Projections within the large acallosal region on the lateral side of V1 were found at two sites; the stronger input was to anterior AL, whereas weaker input was found in LI at the posterior/lateral border of the acallosal region (Fig. 8*B*,*D*). The projection to P was found in a smaller acallosal region behind the one that contained LM, AL, and LI (Fig. 8*B*,*D*). In callosally connected cortex lateral (ventral) to P, we found connections to POR (Fig. 8*B*,*D*). The projections to RL were associated with the callosal ring anterior to the large acallosal region (Fig. 8*B*,*D*). The acallosal cortex between the tip of V1 and S1 contained multiple patches of BDA-labeled axons that terminated in area A (Fig. 8*B*,*D*). In acallosal cortex on the medial side of V1, we found strong inputs to AM and PM (Fig. 8*B*,*D*).

Targets in which we previously found no evidence for visuotopic maps are referred to as regions or fields instead of areas. To identify these targets, we used a combination of SMI-32, m2AChR, and RALDH3 immunostaining as chemical labels. These markers were consistently expressed in distinct, partially overlapping (SMI-32 and m2AChR) (Figs. 5, 6) and sometimes complementary (m2AChR and RALDH3) (Fig. 7) regions with unambiguous borders that were extremely useful for subdividing

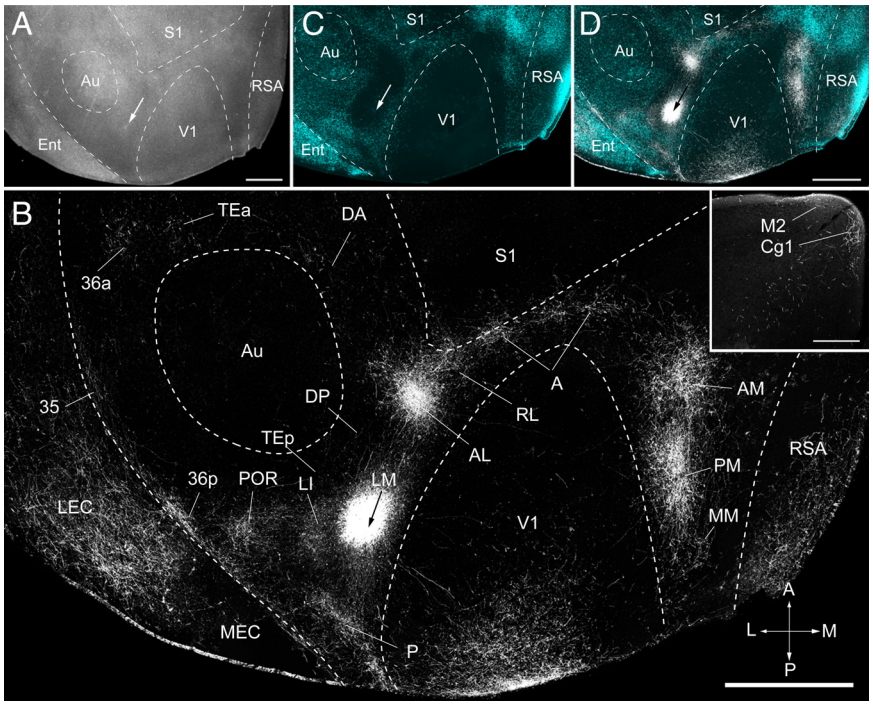

Figure 8. Connections of area LM of adult mouse visual cortex. ***A***, Tangential section through layer 2/3 of left posterior cerebral cortex showing injection site (arrow) in a dark-field image of myeloarchitecture. ***B***, Dark-field image of axonal projections labeled by BDA injection (arrow) into LM. The projections to areas P, POR, LI, AL, RL, A, AM, and PM of the visual cortex are identified by their location relative to fixed retrogradely bisbenzimide-labeled callosal landmarks (Wang and Burkhalter, 2007) shown in the overlay in ***C*** and ***D***. V1, S1, and Au were identified by their distinct myeloarchitectures. RSA, MEC, LEC, Cg1 (inset), and M2 (inset) were identified based on cytoarchitectonic features (Franklin et al., 2007). Projections to TEa, 36p, and 35 were identified by their relative location to SMI-32-, m2AChR-, and RALDH3-labeled/unlabeled regions (see Results for details). DA was identified by its location in the m2AChR-negative region at the dorsal/anterior margin of Au. MM was identified by its location in the SMI-32-negative/m2AChR-negative/RALDH3-positive strip in callosally connected cortex. Ent, Entorhinal cortex; A, anterior; M, medial; P, posterior; L, lateral. Scale bars: ***A***, ***B***, ***D***, 1 mm; ***B***, inset, 0.3 mm.

the relatively featureless cortical sheet. In motor, cingulate, and prelimbic cortex in which labeling with SMI-32, m2AChR, and RALDH3 was less distinctive, targets were identified based on established cytoarchitectonic criteria (Paxinos and Franklin, 2001; Dong, 2008).

In the temporal lobe, we identified projections to field 36 in SMI-32-negative/m2AChR- negative/RALDH3-positive cortex that labeled clusters of axons in anterior 36a, including weak projections to field 35 in the fundus of the rhinal sulcus (Figs. 5–7, 8*B*). Projections to the posterior region 36p overlapped with a small field of SMI-32-negative/m2AChR-positive/RALDH3-postitive cortex in front of POR (Figs. 5–7, 8*B*). Very weak inputs were observed in TEp in SMI-32-negative/m2AChR-negative/RALDH3-positive cortex and the m2AChR-expressing fields of Au, DP, and S2 (supplemental Fig. 1, available at www.jneurosci.org as supplemental material). More consistent inputs were found in TEa and the cortex around the anterior margin of Au (Figs. 5–7, 8*B*).

In parietal cortex, we found extremely weak inputs to the septa of S1 and to the m2AChR-negative DA region at the dorsal/anterior border of Au (Figs. 6, 8*B*).

In medial/posterior cortex, we found weak projections in the acallosal, SMI-32-negative/m2AChR-negative/RALDH3-positive strip, which we designated MM (Figs. 5–7, 8*B*).

In limbic cortex medial to MM, we found inputs that were almost completely confined to RSA and only rarely showed axons in layer 1 of the granular subdivision (Fig. 8*B*). Inputs to other limbic regions in entorhinal cortex terminated more strongly in LEC than in MEC (Fig. 8*B*). The inputs to the presubiculum and subiculum were weak (data not shown).

In frontal cortex, the strongest inputs were found in the primary cingulate area [Cg1 (Paxinos and Franklin, 2001), ACAd (Dong, 2008)] (Fig. 8*B*, inset). In rat, Cg1 represents a motor region in which weak microstimulation elicits eye and eyelid movements (Brecht et al., 2004). Very weak input was found to the neighboring M2 region (Fig. 8*B*, inset), which in rat may correspond to AGm or Fr2 (Palomero-Gallagher and Zilles, 2004) and was shown to contain a motor map for vibrissa movements (Brecht et al., 2004).

Connections to the prefrontal cortex terminated in the dorsal teania tecta of infralimbic cortex (IL) (Van De Werd et al., 2010) (data not shown), which is involved in fear-extinction learning (Hefner et al., 2008) and in rat lacks input from visual cortex (Hoover and Vertes, 2007). Finally, a weak projection was found to the ventral orbitofrontal area (VO; data not shown) which was shown to play a role in navigation and spatial attention (Kolb et al., 1983; King et al., 1989; Corwin et al., 1994; Feierstein et al., 2006).

Connections of area AL

The connections of AL were studied in five mice. In all of these, the injections were in the anterior part of the large acallosal region on the lateral side of V1, which is far away from the LM/AL border. As expected from previous mapping studies (Wang and Burkhalter, 2007), we found that inputs terminated in the upper visual field at the posterior border of V1 (Wang and Burkhalter, 2007), indicating that the injections were centered in AL. In each of these cases, we found labeled projections in similar targets, but the distribution of inputs was dependent on the topographic location of the injection site (Wang and Burkhalter, 2007). For example, injections into the upper periphery of the visual field labeled projections on the posterior/medial side of V1 (Fig. 9*B*). In contrast, more peripheral injections in slightly lower parts of the upper visual field labeled projections along the medial border of V1 [Burkhalter and Wang (2008), their Fig. 20.4]. Similar topographic dependences were found for inputs to extrastriate cortex. Here, the projections to LM terminated at the posterior edge of the acallosal region and almost completely merged with inputs to LI (Fig. 9*B*). Upper peripheral inputs to PM and AM labeled two patches separated by a gap from V1, which shows sparing of the extreme upper peripheral visual field and is consistent with the topography of V1 inputs (Wang and Burkhalter, 2007) (Fig. 9*B*). Similar to inputs from LM, upper field projections of AL terminated in anterior RL, A, P, and POR (Fig. 9*B*).

We were surprised that injections that covered most of AL labeled only a small fraction of V1 projections with striking topographic organization (Fig. 9*B*). Similar labeling patterns were obtained by apparently much smaller injections (Fig. 8*B*; supplemental Fig. 1, available at www.jneurosci.org as supplemental material). These results suggest that the effective site of BDA

uptake of apparently unequal injections was similar and the difference in the size of injection seen in histological sections may be misleading.

AL injections labeled 27 distinct cortical targets that differed in projection strengths. A subset of these targets (V1, P, POR, LI, LM, RL, A, AM, and PM) was previously identified as areas (Wang and Burkhalter, 2007) and was distinguished here by their location relative to callosal landmarks. The remainder of the projections was assigned to SMI-32-, m2AChR-, and RALDH3-positive/negative fields or cytoarchitectonic regions (Paxinos and Franklin, 2001; Dong, 2008).

In the occipital cortex, we found strong projections to LM in the posterior part of the large acallosal region lateral to V1 (Fig. 9*B*,*D*). At the lateral border of the acallosal region, we found a weak projection to LI, which was joined with LM projections at the LM/LI border (Fig. 9*B*,*D*) (Wang and Burkhalter, 2007). A similarly weak and partially overlapping projection was found in the acallosal territory of P (Fig. 9*B*,*D*). The projections from AL to POR, 36p, 36a, Tea, and 35 were substantially weaker than from LM. However, unlike LM, we found that AL sent strong inputs to the SMI-32-negative/m2AChR-negative/RALDH3-positive region in posterior temporal association cortex designated TEp (Figs. 5–7, 9*B*,*D*), which appears to coincide with the ventral auditory field (Storace et al., 2010). In addition, we found moderately strong projections in Au and DP, associated with the SMI-32-positive/m2AChR-positive/RALDH3-negative region of the dorsal auditory belt (Figs. 5–7, 9*B*,*D*).

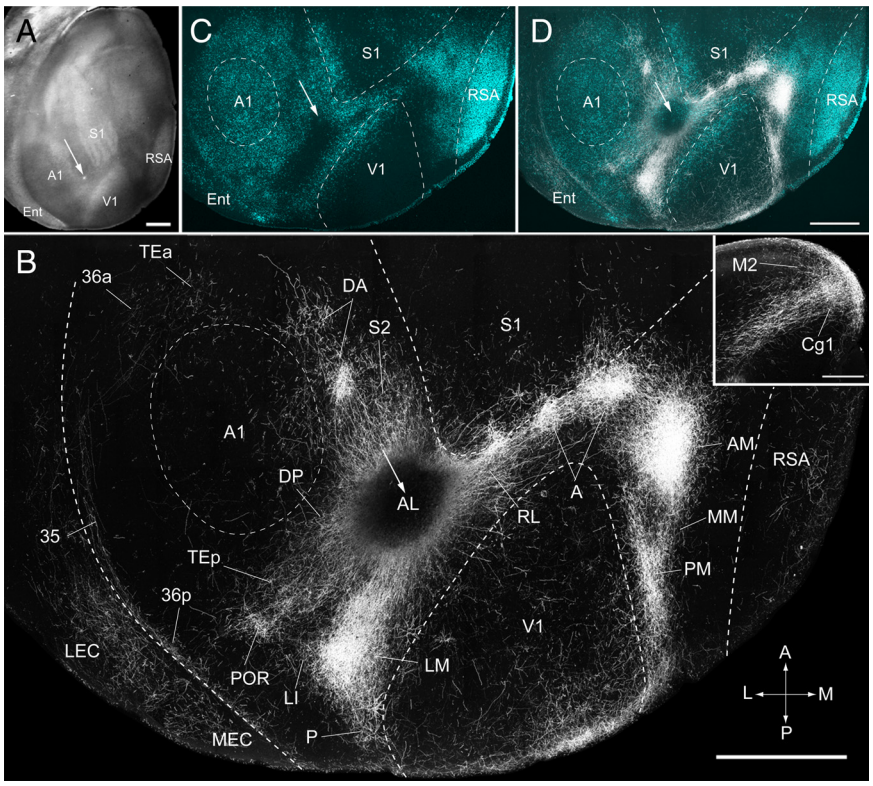

Figure 9. Connections of area AL of adult mouse visual cortex. ***A***, Tangential section through layer 2/3 of left posterior cerebral cortex showing injection site (arrow) in a dark-field image of myeloarchitecture. ***B***, Dark-field image of axonal projections labeled by BDA injection (injection site is dark because of quenching by the brown reaction product) into AL (arrow). ***C***, ***D***, The projections to areas P, POR, LI, LM, RL, A, AM, and PM of the visual cortex are identified by their location relative to retrogradely bisbenzimide-labeled callosal connections (***C***) and overlaying these fixed landmarks on the BDA-labeled projection pattern (***D***). V1, S1, and Au were identified by their distinct myeloarchitectures. RSA, MEC, LEC, Cg1 (inset), and M2 (inset) were identified based on cytoarchitectonic features (Paxinos and Franklin, 2001). S2 was identified based on distinctive m2AChR expression (see Fig. 6*A*). DP was identified as the SMI-32-positive/m2AChR-positive region at the dorsal/posterior edge of Au. DA was identified by location in the m2AChR-negative region at the dorsal/anterior margin of Au. Projections to TE (TEa, TEp), 36 (36p), and 35 were identified by their location relative to SMI-32-, m2AChR-, and RALDH3-labeled/unlabeled regions (see text for details). MM was identified by its location in the m2AChR-negative/RALDH3-positive strip in callosally connected cortex. Ent, Entorhinal cortex; A, anterior; M, medial; P, posterior; L, lateral. Scale bars: ***A***, ***B***, ***D***, 1 mm; ***B***, inset, 0.3 mm.

Parietal cortex received much stronger input from AL than LM. These inputs were targeted to RL, A, the septa and dysgranular zone of S1 (Alloway, 2008), the m2AChR-expressing whisker region of S2 (Aronoff et al., 2010), and the m2AChR-negative multisensory region designated DA (Figs. 6, 9*B*,*D*).

In cortex medial to V1, we found AL projections to PM and extremely strong input to AM, which was much denser than input from LM (Figs. 8*B*, 9*B*,*D*). In contrast, the projections from AL to MM were weaker than from LM (Figs. 8*B*, 9*B*,*D*).

Inputs to limbic cortex terminated almost exclusively in RSA (Fig. 9*B*,*D*). In entorhinal cortex, the projections to the SMI-32-positive/m2AChR-postive MEC were stronger than to the more weakly SMI-32/m2AChR-expressing LEC (Fig. 9*B*,*C*). Inputs to subiculum and presubiculum were weak (data not shown).

Inputs to frontal cortex terminated strongly in Cg1 (Fig. 9*B*). However, unlike LM, AL also projected much more strongly to the medial agranular cortex, which in mice is designated M2 or MOPs (Fig. 9*B*, inset) (Paxinos and Franklin, 2001; Dong, 2008). In rat, M2 may correspond to the medial agranular field (AGm or Fr2) (Brecht et al., 2004), which is part of primary motor cortex where low-threshold microstimulation elicits whisker movements that are important for active sensing of the environment (Brecht et al., 2004; Diamond, 2010).

Input to the prefrontal cortex included the infralimbic field designated IL (Paxinos and Franklin, 2001) (data not shown) or ILA (Dong, 2008) (data not shown). Orbitofrontal projections terminated in VO (data not shown).

Strengths of LM and AL connections

Our qualitative studies of BDA-labeled intracortical connections have shown that AL projects to a larger number of visual, multisensory, and motor targets in temporal, parietal, and frontal cortex than LM, whose connections were more confined to visual and sensory association regions in temporal and occipital cortex. This description, however, is derived solely from the presence or absence of connections, which provides incomplete information about the specificity of the network (Markov et al., 2010) and the flow of visual information through LM and AL. We therefore studied whether the qualitative differences were expressed in the projection strengths. For this, we first determined whether the bouton densities in 10 BDA-labeled targets of V1 were correlated with the optical densities of label in the terminal fields. This was done by using an optical dissector probe for counting boutons and scaling each projection to the sum of boutons labeled in the 10 targets of V1. The results showed that the absolute bouton density differed in the 10 targets (Fig. 10*A*). More importantly,

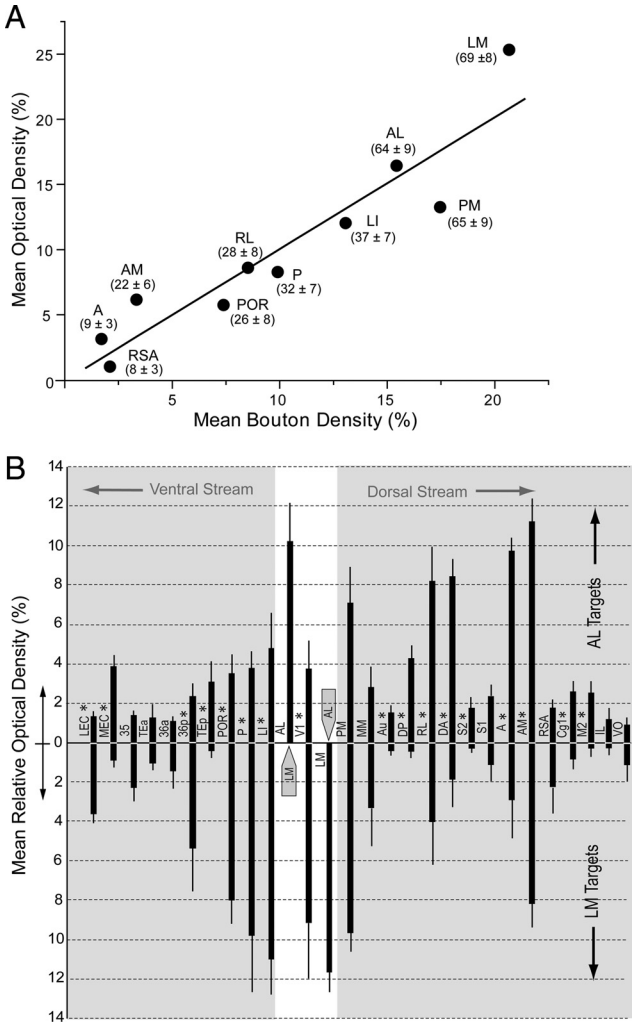

Figure 10. Relative strengths of inputs from areas LM and AL to targets in ventral and dorsal cerebral cortex. ***A***, Positive significant ($R^2 = 0.94$, $p < 0.0001$) correlation between average bouton density (3 fields in layers 2–4 per projection in 3 mice) and average optical density (3 fields in layers 2–4 per projection in 3 mice) of BDA-labeled connections in 10 targets of V1. Numbers in parentheses indicate the average ± SEM number of boutons/100 μm^2 counted in three sections across each projection field in three mice. ***B***, Relative strength (mean optical density/projection as a percentage of the sum of optical densities of all projections ± SEM) of projections from LM (downward facing bars) and AL (upward facing bars) in different targets of the cortex. Projections from LM more strongly innervate targets in temporal cortex, whereas AL more strongly innervates parietal and frontal cortex, suggesting that LM and AL are gateways to ventral (gray region on the left side) and dorsal (gray region on the right side) streams, respectively. Injected areas LM and AL are indicated by gray arrows. *Significant ($p < 0.05$) differences.

we found a highly significant ($R^2 = 0.94$; $p < 0.0001$) positive linear relationship between bouton density and optical density (Fig. 10*A*). This suggests that bouton density is significantly correlated with optical density and that the projection density is independent of the BDA injection site as well as occasional retrogradely labeled neurons in the target area.

We next used densitometry to compare the strengths of BDA-labeled axonal projections from LM and AL. The weight of individual projections were plotted as a percentage of the summed density of all projections labeled in the same mouse and averaged across animals. For optimal visualization, the projection targets were plotted according to their natural location within the cortex. The analysis shows that LM and AL were strongly reciprocally connected with each other (Fig. 10*B*). The results also show that LM and AL shared multiple projection targets but that the strengths of many projections differed between LM and AL. For example, LM showed significantly ($p < 0.01$) stronger feedback connections to V1 than AL (Fig. 10*B*). LM also showed significantly ($p < 0.01$) stronger connections to the temporal areas LI, P, POR, and the LEC ($p < 0.05$) (Fig. 10*B*). In contrast, the connections from AL were significantly ($p < 0.01$) stronger in the parietal areas RL, DA, A, and AM as well as MEC ($p < 0.05$). In addition, AL sent significantly stronger input to the auditory areas Au, DP, and TEp; S2; the primary motor whisker cortex (M2); and the frontal eye field (Cg1) (Fig. 10*B*). These quantitative results strongly support the notion that information from LM preferentially flows in a ventral stream of interconnected areas, whereas AL is preferentially connected to a dorsal stream. Although such streams suggest functional segregation, it is important to note that we found connections between each of the 10 injected areas, indicating a high degree of integration within the visual cortical network.

Discussion

We have found that LM and AL have distinct cytoarchitectures and chemoarchitectures and project to diverse sets of cortical targets. Quantitative analyses show that LM projects more strongly to temporal than to parietal and frontal areas, whereas AL's outputs are stronger to parietal and frontal than to temporal areas. The results support previous findings that LM and AL contain separate topographic maps of the visual field (Wang and Burkhalter, 2007) and process different stimulus features (Gao et al., 2006). Thus, all criteria are met for regarding LM and AL as distinct areas, acting as gateways of ventral and dorsal visual processing streams. Alternative schemes that lump LM and AL into a single area, V2L, do not reflect the true structure of mouse visual cortex in which V1 is adjoined by a string of small areas (Schuett et al., 2002; Wang and Burkhalter, 2007; Tohmi et al., 2009) and misrepresent V2L as a single area, homologous to primate V2 (Rosa and Krubitzer, 1999; Kalatsky and Stryker, 2003; Van den Bergh et al., 2010).

Ventral and dorsal stream

Previous studies of the cytoarchitectonic field known as 18a, Oc2L, and V2L (Caviness, 1975; Paxinos and Watson, 1986; Franklin and Paxinos, 2007) have shown in rat and mouse that the region is reciprocally connected with occipital, temporal, parietal, and frontal cortex (Beckstead, 1979; Simmons et al., 1982; Miller and Vogt, 1984; Reep et al., 1990; Paperna and Malach, 1991; Shi and Casell, 1997; Burwell and Amaral, 1998). Although differences in the projections of anterior and posterior lateral extrastriate cortex were observed previously, they were considered experimental variations. A few studies, however, noted that the posterior part of rat Oc2L is more strongly linked to temporal cortex and the amygdala than the anterior part, which provides stronger input to the parietal cortex but lacks connections with the amygdala (Sanderson et al., 1991; McDonald and Mascagni, 1996). Sanderson et al. (1991) first suggested that these patterns were not variations but represent the connections of distinct areas LM and AL. This proposal was supported by findings in rat, showing that AL more strongly projects to S1 and S2 and is higher in the hierarchy than LM (Coogan and Burkhalter, 1993). We found similar differences in mouse and show, using more definitive areal identifications, that LM has much weaker inputs to TEp, Au, DP, DA, and S2, which are important targets of AL. Our results also show quantitative differences in projections that are shared by AL and LM, demonstrating that LM is more strongly

connected to V1 and the temporal areas P, LI, and POR. In contrast, AL has stronger connections with posterior parietal (RL, A, AM) and motor (M2, Cg1) areas and favors MEC over LEC. The preferential flow of information from LM into the ventral stream is consistent with findings in rat, showing that the postrhinal area (POR), which is connected to areas LM and AL, receives 33% of its input from medial and lateral extrastriate cortex (Burwell and Amaral, 1998). In contrast, information from posterior parietal cortex, which is a major target of AL that is strongly connected to the dorsal processing stream, sends only 7% of inputs to POR (Burwell and Amaral, 1998). The connection patterns suggest that LM and AL belong to distinct but interconnected visual processing streams. However, it is important to note that the relationship between anatomical weight and physiological efficacy of connections is complex (Ahmed et al., 1994; Binzegger et al., 2004), indicating that additional studies will be necessary to determine whether the static organization corresponds to the functional network.

Functional differences of ventral and dorsal streams

LM and AL receive retinal information from subcortical centers and via connections from V1. Subcortical inputs to LM ascend directly via the lateral geniculate nucleus and indirectly via the superior colliculus (SC) and lateral the posterior thalamus (LP) (Masterson et al., 2009; Wang and Burkhalter, 2009). In contrast, subcortical inputs to AL are carried exclusively by the indirect SC→LP pathway (Simmons et al., 1982; Wang and Burkhalter, 2009). These differences may account for the longer latencies of responses in AL than LM (Gao et al., 2008). The cortical inputs from V1 to LM and AL are similar in length, but they derive from distinct populations of neurons (Wang and Burkhalter, 2005), resembling the organization of rat V1 in which separate groups of neurons project to extrastriate visual, auditory, and somatosensory cortices (Paperna and Malach, 1991). Optical recordings in cat V1 have shown that functionally different sets of neurons reside in distinct clusters (Shoham et al., 1997), which in monkey project to functionally discrete compartments in V2 (Sincich et al., 2007, 2010; Chen et al., 2008; Kaskan et al., 2009). A similar organization may exist in mouse V1 in which LM-projecting neurons are specialized for the processing of high spatial frequency/high-contrast information, whereas AL-projecting neurons are optimally tuned to low spatial frequency/low-contrast stimuli (Gao et al., 2010). Such differential targeting of inputs may account for LM neurons that are tuned to high spatial frequency and slow speed and AL neurons that are more sensitive to low spatial frequency and high speed of motion (Montero and Jian, 1995; Gao et al., 2006).

The channeling of nonspatial and spatial information from LM and AL, optimized for signaling object attributes and target location, respectively, resembles the distinction into ventral and dorsal streams known in primate visual cortex (Ungerleider and Mishkin, 1982; Nassi and Callaway, 2009). A similar organization was proposed from studies in rats, which showed that lesions in the dorsal posterior parietal cortex impaired visuospatial perception (Kolb et al., 1982; Kolb and Walkey, 1987). In contrast, lesions in the ventral extrastriate visual cortex showed impairments in pattern discrimination (Gallardo et al., 1979; Dean, 1981; McDaniel et al., 1982). Moreover, studies in rat have shown that damaging temporal cortex, downstream of the main outflow of LM, disrupted object recognition but spared spatial memory (Bussey et al., 1999; Prusky et al., 2004; Davies et al., 2006). One interpretation of our results, then, is that LM projections play a role in object recognition, whereas AL inputs are important for the construction of spatial maps.

Although the segregation into dorsal and ventral streams may play a role for visual perception, it is important to note that this organization also sheds light on the layout of the network for spatial navigation that includes the entorhinal–hippocampal circuit and the posterior parietal cortex (Burwell and Amaral, 1998; Whitlock et al., 2008). Specifically, our results suggest that POR, which is thought to relay output from grid cells in MEC (Fhyn et al., 2004; Haftig et al., 2005) to posterior parietal cortex (Whitlock et al., 2008), receives much stronger inputs from LM than AL. This may explain why the spatial modulation of POR neurons is weak and unstable (Burwell and Hafeman, 2003; Fhyn et al., 2004; Gaffan et al., 2004). Our results also suggest that the MEC, whose grid cells signal self-position (Fhyn et al., 2004; Haftig et al., 2005) and sends input to posterior parietal cortex, receives stronger input from AL than LM. Thus, it is likely that the visual motion information from AL (Gao et al., 2006) provides self-motion cues (Maunsell and Van Essen, 1983) over a range of running speeds (Meek et al., 2009) to MEC. In addition, AL also provides input to auditory, somatosensory, and polymodal areas in posterior parietal cortex (Toldi et al., 1986; Nakamura, 1999; Brett-Green et al., 2003). This input may be important for aligning external visual and auditory coordinates, with body-centered somatosensory, proprioceptive, and vestibular maps required for path integration and transformation of the self-location into goal-directed behavior (Chen et al., 1994; Whitlock et al., 2008). Unsurprisingly, disruption of visual and somatosensory integration in rat posterior parietal cortex interferes with path integration and results in disorientation (Pinto-Hamuy et al., 1987; Save and Poucet, 2000).

Dorsal and ventral stream inputs to temporal and entorhinal cortex

We have found that the connections from LM to LEC are stronger than from AL. Conversely, we have found that inputs to MEC arise principally from AL. This network differs from rat, where lateral extrastriate visual cortex provides the principle input to POR and few connections go to area 36 (Burwell and Amaral, 1998). Unlike in mouse, most connections of rat visual cortex terminate in MEC, whereas LEC receives little visual input (Witter and Amaral, 2004). These results suggest that nonspatial inputs about object attributes and spatial information about object location flow to both POR and perirhinal cortex. In addition, the network in mouse suggests that the weakly spatially selective LEC (Hargreaves et al., 2005) receives both spatial and nonspatial inputs from the ventral stream, whereas the grid cell-containing MEC (Fhyn et al., 2004; Haftig et al., 2005) receives mainly spatial input from the dorsal stream. Thus, convergent inputs from LEC and MEC to the hippocampus may create representations of objects and place that resemble episodic memory (Knierim et al., 2006).

References

Ahmed B, Anderson JC, Douglas RJ, Martin KAC, Nelson JC (1994) Polyneuronal innervation of spiny stellate neurons in cat visual cortex. J Comp Neurol 341:39–49.

Alloway KD (2008) Information processing stream in rodent barrel cortex: the differential functions of barrel and septal circuits. Cereb Cortex 18:979–989.

Aronoff R, Matyas F, Mateo C, Ciron C, Schneider B, Petersen CC (2010) Long-range connectivity of mouse primary somatosensory barrel cortex. Eur J Neurosci 31:2221–2233.

Beckstead RM (1979) An autoradiographic examination of corticocortical

and subcortical projections of the mediodorsal-projection (prefrontal) cortex in the rat. J Comp Neurol 184:43–61.

Benison AM, Rector DM, Barth DS (2007) Hemispheric mapping of secondary somatosensory cortex in the rat. J Neurophysiol 97:200–2007.

Binzegger T, Douglas RJ, Martin KAC (2004) A quantitative map of the circuit of cat primary visual cortex. J Neurosci 24:8411–8453.

Bird CM, Burgess N (2008) The hippocampus and memory: insights from spatial processing. Nat Rev Neurosci 9:182–194.

Brecht M, Krauss A, Muhammad S, Sinai-Esfahani L, Bellanca S, Margerie TW (2004) Organization of rat vibrissa motor cortex and adjacent areas according to cytoarchitectonics, microstimulation, and intracellular stimulus of identified cells. J Comp Neurol 479:360–373.

Brett-Green B, Fifková E, Larue DT, Winer JA, Barth DS (2003) A multisensory zone in rat parietotemporal cortex: intra- and extracellular physiology and thalamocortical connections. J Comp Neurol 460:223–237.

Budinger E, Scheich H (2009) Anatomical connections suitable of the direct processing of neuronal information of different modalities via the rodent primary auditory cortex. Hear Res 258:16–27.

Burkhalter A, Wang Q (2008) Interconnections of visual cortical area in the mouse. In: Eye, retina, and visual system of the mouse (Chalupa LM, Williams RW, eds), pp 245–254. Cambridge, MA: Massachusetts Institute of Technology.

Burwell RD (2000) The parahippocampal region: corticocortical connectivity. Ann N Y Acad Sci 911:25–42.

Burwell RD, Amaral DG (1998) Cortical afferents of the perirhinal, postrhinal, and entorhinal cortices of the rat. J Comp Neurol 398:179–205.

Burwell RD, Hafeman DM (2003) Positional firing properties of postrhinal cortex neurons. Neuroscience 119:577–588.

Bussey TJ, Muir JL Aggleton JP (1999) Functionally dissociating aspects of event memory he effects of combined perirhinal and postrhinal cortex lesions of object and place memory in the rat. J Neurosci 19:495–502.

Carvell GE, Simons DJ (1986) Somatotopic organization of the second somatosensory area (SII) in the cerebral cortex of the mouse. Somatosens Res 3:213–237.

Caviness VS (1975) Architectonic map of neocortex of the mouse. J Comp Neurol 164:247–264.

Chen G, Lu HD, Roe AW (2008) A map for horizontal disparity in monkey V2. Neuron 58:442–450.

Chen LL, Lin L-H, Barnes CA, McNaughton BL (1994) Head-direction cells in the rat posterior cortex. II. Contributions of visual and ideothetic information to the directional firing. Exp Brain Res 101:24–34.

Coogan TA, Burkhalter A (1993) Hierarchical organization of areas in rat visual cortex. J Neurosci 13:3749–3772.

Corwin JV, Fussinger M, Meyer RC, King VR, Reep RL (1994) Bilateral destruction of the ventrolateral orbital cortex produces allocentric but not egocentric spatial deficits in rats. Behav Brain Res 61:79–86.

Davies M, Machin PE, Sanderson DJ, Pearce JM, Aggleton JP (2007) Neurotoxic lesions of the rat perirhinal cortices and their impact on biconditional visual discrimination tasks. Behav Brain Res 176:274–283.

Dean P (1981) Visual pathways and visual acuity in hooded rats. Behav Brain Res 3:239–271.

Diamond ME (2010) Texture sensation though finger tips and the whiskers. Curr Opin Neurobiol 20:319–327.

Doeller CF, Barry C, Burgess N (2010) Evidence for grid cells in a human memory network. Nature 463:657–661.

Dong HW (2008) Allen reference atlas. Seattle: Wiley.

Dräger UC (1975) Receptive fields of single cells and topography in mouse visual cortex. J Comp Neurol 160:269–290.

Eichenbaum H, Lipton PA (2008) Towards a functional organization of the medial temporal lobe memory system: role of the parahippocampus and medial entorhinal cortical areas. Hippocampus 18:1314–1324.

Eickhoff SB, Rottschy C, Kujovic M, Palomero-Gallagher N, Zilles K (2008) Organizational principles of human visual cortex revealed by receptor mapping. Cereb Cortex 18:2637–2645.

Fabri M, Burton H (1991) Ipsilateral cortical connections of primary somatic sensory cortex in rats. J Comp Neurol 311:405–424.

Feierstein CE, Quirk MC, Uchida N, Sosulski DL, Mainen ZF (2006) Representation of spatial goals in rat orbitofrontal cortex. Neuron 51:495–507.

Felleman DJ, Van Essen DC (1991) Distributed hierarchical processing in the primate cerebral cortex. Cereb Cortex 1:11–47.

Franklin KBJ, Paxinos G, Watson C (2007) The mouse brain in stereotaxic coordinates. Amsterdam: Elsevier.

Fyhn M, Molden S, Witter MP, Moser EI, Moser MB (2004) Spatial representation in the entorhinal cortex. Science 305:1258–1264.

Gaffan EA, Healey AN, Eacott MJ (2004) Objects and positions in visual scenes: effects of perirhinal and postrhinal cortex lesions in the rat. Behav Neurosci 188:1142–1148.

Gallardo L, Mottles M, Vera L, Carrasco MA, Torrealba F, Montero VM, Pinto-Hamuy T (1979) Failure by rat to learn a visual conditional discrimination after lateral peristriate cortical lesions. Physiol Psychol 7:173–177.

Gao E, DeAngelis CD, Burkhalter A (2006) Specialized areas for shape and motion analysis in mouse visual cortex. Soc Neurosci Abstr 32:641.6.

Gao E, DeAngelis CD, Burkhalter A (2008) Visual response latencies in different areas of mouse visual cortex. Soc Neurosci Abstr 34:853.17.

Gao E, DeAngelis GC, Burkhalter A (2010) Parallel input channels to mouse primary visual cortex. J Neurosci 30:5912–5926.

Goodale MA (2011) Transforming vision into action. Vis Res, in press.

Gordon JA, Stryker MP (1996) Experience-dependent plasticity of binocular responses in the primary visual cortex of the mouse. J Neurosci 16:3274–3286.

Haftig T, Fyhn M, Molden S, Moser MB, Moser EI (2005) Microstructure of a spatial map in the entorhinal cortex. Nature 436:801–806.

Hamasaki T, Leingärtner A, Ringstedt T, O'Leary DDM (2004) Emx2 regulates sizes and positioning of the primary sensory and motor areas in neocortex by direct specification of cortical progenitors. Neuron 43:359–372.

Hargreaves EL, Rao G, Lee I, Knierim JJ (2005) Major dissociation between medial and lateral entorhinal input to dorsal hippocampus. Science 308:1792–1794.

Hefner K, Whittle N, Juhasz J, Norcross M, Karlsson RM, Sakida LM, Bussey TJ, Singewald N, Holmes A (2008) Impaired fear extinction learning and cortico-amygdala circuit abnormalities in a common genetic mouse strain. J Neurosci 28:8074–8085.

Higgins NC, Storace DA, Escabi MA, Read HL (2010) Specialization of binaural responses in ventral auditory cortices. J Neurosci 30:14522–14532.

Hoover WB, Vertes RP (2007) Anatomical analysis of afferent projections to the medial prefrontal cortex in the rat. Brain Struct Funct 212:149–179.

Jiang X, Johnson RR, Burkhalter A (1993) Visualization of dendritic morphology of cortical projections neurons by retrograde labeling. J Neurosci Methods 50:45–60.

Kalatsky VA, Stryker MP (2003) New paradigm for optical imaging: temporally encoded maps of intrinsic signal. Neuron 38:529–545.

Kaskan PM, Lu HD, Dillenburger BC, Kaas LH, Roe AW (2009) The organization of the orientation-selective, luminance-change and binocular preference domains in the second (V2) and third (V3) visual areas of New World monkeys as revealed by intrinsic optical imaging. Cereb Cortex 19:1394–1407.

King VR, Corwin JV, Reep RL (1989) Production and characterization of neglect in rats with unilateral lesions of ventrolateral orbital cortex. Exp Neurol 105:287–299.

Knierim JJ, Lee I, Hargreaves EL (2006) Hippocampal place cells: parallel input streams, subregional processing, and implications for episodic memory. Hippocampus 16:755–764.

Kolb B (1990) Posterior parietal and temporal association cortex. In: The cerebral cortex of the rat (Kolb B, Tees RC, eds), pp 459–472. Cambridge, MA: Massachusetts Institute of Technology.

Kolb B, Walkey J (1987) Behavioral and anatomical studies of the posterior parietal cortex in the rat. Behav Brain Res 23:127–145.

Kolb B, Sutherland RJ, Whishaw IQ (1983) A comparison of the contributions of the frontal and parietal association cortex to spatial localization in rats. Behav Neurosci 97:13–27.

Luo T, Wagner E, Grün F, Dräger UC (2004) Retinoic acid signaling in the brain marks formation of optic projections, maturation of the dorsal telencephalon, and function of limbic sites. J Comp Neurol 470:297–316.

Markov NT, Misery P, Falchier A, Lamy C, Vezoli J, Quilodran R, Gariel MA, Giroud P, Ercsey-Ravasz, Pilaz LJ, Huissoud C, Barone P, Dehay C, Toroczkai Z, Van Essen DC, Kennedy H, Knoblauch K (2011) Weight consistency specifies regularities of macaque networks. Cereb Cortex, in press.

Masterson SP, Li J, Bickford ME (2009) Synaptic organization of the tec-

torecipient zone of the rat lateral posterior nucleus. J Comp Neurol 515:647–663.

Maunsell JHR, Van Essen DC (1983) Functional properties if neurons in the middle temporal visual area of the macaque monkey. I. Selectivity for stimulus direction, speed, orientation. J Neurophysiol 69:19–39.

McDaniel WF, Coleman J, Lindsay JF Jr (1982) A comparison of lateral peristriate and striate neocortical ablations in the rat. Behav Brain Res 6:249–272.

McDonald AJ, Mascagni F (1996) Cortico-cortical and cortico-amygdaloid projections of the rat occipital cortex: a *Phaseolus vulgaris* leucoagglutinin study. Neuroscience 71:37–54.

Meek TH, Lonquich BP, Hannon RM, Garland T Jr (2009) Endurance capacity of mice selectively bred for high voluntary wheel running. J Exp Biol 212:2908–2917.

Miller MW, Vogt BA (1984) Direct connections of rat visual cortex with sensory, motor, and association cortices. J Comp Neurol 226:184–202.

Montero VM, Jian S (1995) Induction of *c-fos* protein by patterned visual stimulation in central pathways of the rat. Brain Res 690:189–199.

Nakamura K (1999) Auditory spatial discriminatory and mnemonic neurons in rat posterior parietal cortex. J Neurophysiol 82:2503–2517.

Nassi JJ, Callaway EM (2009) Parallel processing strategies of the primate visual system. Nat Rev Neurosci 10:360–372.

Olavarria J, Montero VM (1989) Organization of visual cortex in the mouse revealed by correlating callosal and striate-extrastriate connections. Vis Neurosci 3:59–69.

Palomero-Gallagher N, Zilles K (2004) Isocortex. In: The rat nervous system, (Paxinos G, ed), pp 729–757. Amsterdam: Elsevier.

Paperna T, Malach R (1991) Patterns of sensory intermodality relationships in the cerebral cortex of the rat. J Comp Neurol 308:432–456.

Paxinos G, Franklin KBJ (2001) The mouse brain in stereotaxic coordinates. San Diego: Academic.

Paxinos G, Watson C (1986) The rat brain in stereotaxic coordinates. Sydney: Academic.

Pinto-Hamuy T, Olavarria J, Guic-Robles E, Morgues M, Nassal O, Petit D (1987) Rats with lesions in anteromedial extrastriate cortex fail to learn a visuosomatic conditional response. Behav Brain Res 25:221–231.

Prusky GT, Douglas RM, Nelson L, Shabanpoor A, Sutherland RJ (2004) Visual memory task for rats reveals an essential role for hippocampus and perirhinal cortex. Proc Natl Acad Sci U S A 101:5064–5068.

Reep RL, Goodwin GS, Corwin JV (1990) Topographic organization in the corticocortical connections of medial agranular cortex in rats. J Comp Neurol 294:262–280.

Remple MS, Henry EC, Catania KC (2003) Organization of somatosensory cortex in the laboratory rat (*Rattus norvegicus*): evidence for two lateral areas joined at the representation of the teeth. J Comp Neurol 467:105–118.

Rosa MGP, Krubitzer LA (1999) The evolution of visual cortex: where is V2? Trends Neurosci 22:242–248.

Rubinov M, Sporns O (2010) Complex network measures of brain connectivity: used and interpretations. Neuroimage 52:1059–1069.

Saleem KS, Price JL, Hashikawa T (2007) Cytoarchitectonic and chemoarchitectonic subdivisions of the perirhinal and parahippocampal cortices in macaque monkeys .J Comp Neurol 500:973–1006.

Sanderson KJ, Dreher B, Gayer N (1991) Prosencephalic connections of striate and extrastriate areas of rat visual cortex. Exp Brain Res 85:324–334.

Save E, Poucet B (2000) Hippocampal-parietal cortical interactions in spatial cognition. Hippocampus 10:491–499.

Schuett S, Bonhoeffer T, Hübener M (2002) Mapping retinotopic structure in mouse visual cortex with optical imaging. J Neurosci 22:6549–6559.

Shi C-J, Cassell MD (1997) Cortical, thalamic, and amygdaloid projections of rat temporal cortex. J Comp Neurol 383:153–175.

Shoham D, Hübener M, Schulze S, Grinvald A, Bonheoffer T (1997) Spatiotemporal frequency domains and their relation to cytochrome oxidase staining in cat visual cortex. Nature 385:529–533.

Sia Y, Bourne JA (2008) The rat temporal association cortical areas 2 (TE2) comprises tow subdivisions that are visually responsive and develop independently. Neuroscience 156:118–128.

Simmons PA, Lemmon VA, Pearlman AL (1982) Afferent and efferent connections of the striate and extrastriate visual cortex of the normal and reeler mouse. J Comp Neurol 211:295–308.

Sincich LC, Jocson CM, Horton JC (2007) Neurons in V1 patch columns project to thin stripes. Cereb Cortex 17:935–941.

Sincich LC, Jocson CM, Horton JC (2010) V1 interpatch projections to V2 thick stripes and pale stripes. J Neurosci 30:6963–6974.

Stiebler I, Neulist R, Fichtel I, Ehret G (1997) The auditory cortex of the house mouse: left-right differences, tonotopic organization and quantitative analysis of frequency representation. J Comp Physiol A Neuroethol Sens Neural Behav Physiol 181:559–571.

Storace DA, Higgins NC, Read HL (2010) Thalamic labeling patterns suggest primary and ventral auditory fields are distinct core regions. J Comp Neurol 518:1630–1646.

Tohmi M, Takahashi K, Yubota Y, Hishida R, Shibuki K (2009) Transcranial flavoprotein fluorescence imaging of mouse cortical activity and plasticity. J Neurochem 109 [Suppl 1]:3–9.

Toldi J, Feher O, Wolff JR (1986) Sensory interactive zones in the rat cerebral cortex. Neuroscience 18:461–465.

Ungerleider LG, Mishkin M (1982) Two cortical visual systems. In: Analysis of visual behavior (Ingle DJ, Goodale MA, Mansfield RJW, eds), pp 549–586. Cambridge, MA: Massachusetts Institute of Technology.

Van den Bergh G, Zhang B, Arckens L, Chino YM (2010) Receptive-field properties of V1 and V2 neurons in mice and macaque monkeys. J Comp Neurol 518:2051–2070.

Van der Gucht E, Hof PR, Brussel L, Burnat K, Arckens L (2007) Neurofilament protein and neuronal activity markers define regional architectonic parcellation in the mouse visual cortex. Cereb Cortex 17:2805–2819.

Van De Werd HJJM, Rajowska G, Evers P, Uylings HBM (2010) Cytoarchitectonic and chemoarchitectonic characterization of the prefrontal cortical areas in the muse. Brain Struct Funct 214:339–353.

van Groen T (2001) Entorhinal cortex of the mouse: cytoarchitectonical organization. Hippocampus 11:397–407.

Wagner E, Luo T, Sakai Y, Parada LF, Dräger UC (2006) Retinoic acid delineates the topography of neuronal plasticity in postnatal cerebral cortex. Eur J Neurosci 24:329–340.

Wagor E, Mangini NJ, Pearlman AL (1980) Retinotopic organization of striate and extrastriate visual cortex in the mouse. J Comp Neurol 193:187–202.

Wallace MN (1987) Histochemical demonstration of sensory maps in the rat and mouse cerebral cortex. Brain Res 418:178–182.

Wang Q, Burkhalter A (2005) Separate output streams from V1 to higher areas of mouse visual cortex. Soc Neurosci Abstr 31:854.1.

Wang Q, Burkhalter A (2007) Area map of mouse visual cortex. J Comp Neurol 502:339–357.

Wang Q, Burkhalter A (2009) Stream-specific corticothalamic feedback projections in mouse visual cortex. Soc Neurosci Abstr 35:453.19.

Wang Q, Gao E, Burkhalter A (2007) In vivo transcranial imaging of connections in mouse visual cortex. J Neurosci Methods 159:268–276.

Whitlock JR, Sutherland RJ, Witter MP, Moser M-B, Moser EI (2008) Navigating from hippocampus to parietal cortex. Proc Natl Acad Sci U S A 105:14755–14762.

Witter PM, Amaral DG (2004) Hippocampal formation. In: The rat nervous system (Paxinos G, ed), pp 637–687. Amsterdam: Elsevier.